

ENGINEERING PERSPECTIVE**CONTENTS****Research Articles****Page Number**

Müjdat ERSARI, Murat GÜNDOĞDU Tractor Transmission Gear Ratio Optimization	95-99
İrem TANIS, Turan Alp ARSLAN, Tolga KOCAKULAK, Gülşen TASKIN, Tuğba TABANLIGIL CALAM, Hamit SOLMAZ Fabrication and Characterization of Sulfonated Polysulfone Membrane with Different Thicknesses for Proton Exchange Membrane Fuel Cell	100-107
Quang Truc DAM, Fatima HAIDAR, Nour MAMA, Sherwin Joy CHENNAPALL Modeling and simulation of an Internal Combustion Engine using Hydrogen: A MATLAB implementation approach	108-118
M. Kubilay ASKERDEN, Mustafa YAZAR, Şükrü TALAS Effects of CNC Tool Runouts on Drilling Process	119-124
Nikita JAIN, Manish GAUR, Priyanka AGRAWAL, Praveen Kumar DADHEECH A Study of Modified Nanofluid Flow Over an Exponentially Stretching Surface With Inclined Magnetic Field and Porous Media	125-129

**ENGINEERING
PERSPECTIVE****An International Journal****Volume: 4****Issue: 3****30 September 2024****ENGINEERING PERSPECTIVE****Volume: 4****Issue: 3****30 September 2024**

e-ISSN: 2757-9077

Open Access

ENGINEERING PERSPECTIVE

An International Journal

Publishing Manager
Prof. Dr. Hamit SOLMAZ

Editor
Assoc. Prof. Dr. Alper CALAM

Subject Editors

Dr. Lina Montuori, Universitat Politècnica de València (UPV), Spain
Dr. Gang Li, Mississippi State University, USA
Dr. Xing Zheng Wu, Hebei University in Baoding, China
Dr. Mamdouh El Haj Assad, University of Sharjah, United Arab Emirates
Dr. Anle Mu, Xi'an University of Technology, China
Dr. Gulsen Taskin, Gazi University, Türkiye
Dr. Anderson Chu, Columbia University, USA
Dr. Diego Fettermann, Federal University of Santa Catarina (UFSC), Brazil
Dr. Sivasankaran Sivanandam, King Abdulaziz University, Kingdom of Saudi Arabia
Dr. Aniefiok Livinus, University of Uyo, Nigeria
Dr. Murat Akin, Gazi University, Türkiye
Dr. Seyed Mohammad Safieddin Ardebili, Shahid Chamran University of Ahvaz, Iran
Dr. Gultekin Uzun, Gazi University, Türkiye
Dr. Babak Keykhosro Kiani, International Institute of Earthquake Engineering and Seismology, Iran
Dr. Mingjun Xu, Nanyang Technological University, Singapore
Dr. Malek Hassanpour, Osmania University, India
Dr. Seyfettin Vadi, Gazi University, Türkiye

Editorial Board

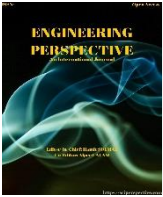
Dr. J. Sadhik Basha, National University of Science & Technology (IMCO), Oman
Dr. Farzad Jaliliantabar, Universiti Malaysia Pahang, Malaysia
Dr. Bakenaz A. Zeidan, Tanta University, Egypt
Dr. Roohollah Zanganeh, Iran University of Science and Technology (IUST), Iran
Dr. Praveen Kumar Dadheech, Rajasthan Technical University Kota, India
Dr. Behrouz Khoshbakht Irdmousa, Michigan Technological University, USA
Dr. N. Shivakumar, Aarupadai Veedu Institute of Technology, India
Dr. Tamilselvan Pachiannan, Jiangsu University, China
Dr. Andrei Alexandru Boroiu, University of Pitesti, Romania
Dr. Tugba Tabanligil Calam, Gazi University, Türkiye
Dr. Kamran Poorghasemi, Islamic Azad University, Iran
Dr. Omar Bait, University of Batna, Algeria
Dr. Anilkumar Shere, Indian Institute of Technology Delhi, India
Dr. Sujit Kumar Verma, GLA University, India
Dr. Seyfi Polat, Hitit University, Türkiye
Dr. Freddie Inambao, University of KwaZulu-Natal, South Africa
Dr. Ridha Ennetta, Gabes University, Tunisia
Dr. Mohammad Amini, University of Saskatchewan, Canada

Language Editor

Neslihan Turan, Kocaeli University, Türkiye

Volume: 4	Issue: 3	30 September 2024
Engineering Perspective publishes four issues per year.		

REVIEWERS WHO CONTRIBUTED TO THIS ISSUE (VOLUME: 4 ISSUE: 3)	
Dr. Can Çivi	Dr. Ömer Karabıyık
Dr. Recep Akkaya	Dr. Merve Keskin
Dr. Antoine Hugo	Dr. Samet Çelebi
Dr. Özgür Özdilli	Dr. Gültekin Uzun
Dr. Merdin Danışmaz	Dr. Edip Taşkesen
<u>Correspondence Address :</u> Gazi University, Faculty of Technology, Department of Automotive Engineering, Teknikokullar - Ankara, TURKIYE	
<u>e-mail:</u> engineering@sciperspective.com	
<u>Technical Editor:</u> Regaip Menküç Gazi University	
<u>Layout Editors:</u> İrem Tanış, Gazi University Zehra Ebrar Ağca, Gazi University	



Tractor Transmission Gear Ratio Optimization

Müjdat Ersari^{1*} , Murat Gündoğdu² 

^{1,2}TürkTraktör Ziraat Makineleri A.Ş., İstanbul, Turkey

ABSTRACT

This study investigates the optimization of gear ratios for a 2-speed transmission, with a focus on enhancing performance and efficiency in diverse operating conditions. Specifically, the research addresses the need for two distinct gears: one optimized for field use and the other for road use. The goal is to improve the versatility and functionality of the transmission system, ensuring that it meets the demands of both rugged terrains and smooth highways. To achieve this, the study employed the company's lifetime test simulation to fine-tune the gear ratios, optimizing them for the most effective power delivery. A significant aspect of the research is the exploration of the transition from a traditional combustion engine tractor, which typically requires multiple gear ratios, to an electric motor setup with only two gears. This transition is made feasible by the electric motor's ability to deliver high torque across a broad RPM range, thereby enhancing performance while reducing the complexity of gear selection. The results of this optimization process show marked improvements in both the transmission's efficiency and its adaptability, making it highly suitable for a range of applications. This research offers valuable insights into the future of transmission design, particularly in the fields of agriculture and transportation, where there is a growing need for systems that are both efficient and versatile.

Keywords: Electrified Powertrain; Gear Ratio Optimization; Tractor Gearbox Design

History

Received: 21.04.2024

Accepted: 18.08.2024

How to cite this paper:

Author Contacts

*Corresponding Author

e-mail addresses: mujdat.ersari@turktraktor.com.tr, murat.gundogdu@turktraktor.com.tr

Ersari, M., Gündoğdu, M. (2024). Tractor Transmission Gear Ratio Optimization. Engineering Perspective, 4 (3), 95-99. <http://dx.doi.org/10.29228/eng.pers.76998>

1. Introduction

The worldwide growing demand for food is pushing the agricultural field towards new innovative solutions to increase the efficiency and productivity of cultivations [1]. The automotive industry is currently experiencing a profound transformation towards sustainable mobility solutions, driven by the urgent need to curb carbon emissions and enhance energy efficiency. Just looking at the production of greenhouse gases (GHG), agricultural activities are responsible for almost 30% of the overall CO₂ production, with a possible increase following the growing demand for more food to sustain the population growth [2,3]. The significant impact of emissions from agricultural machinery has necessitated the gradual implementation of increasingly stringent transnational regulations on pollutant emissions [4]. These directives restrict the permissible levels of pollutants in exhaust gases. To comply with these regulations, contemporary diesel engine manufacturers have adopted various methods, including different types of filters, catalytic systems, and recirculation strategies, to minimize pollutants in the exhaust stream [5,6]. In this evolving landscape, transmission technologies

emerge as crucial elements in optimizing vehicle performance and fuel economy across diverse operational contexts.

This study explores into the process of optimizing gear ratios for tractor transmissions, specifically addressing the transition from conventional combustion engines to electric motors.

Dual-mode tractor transmissions, tailored with gears for both field and road applications, necessitate meticulous optimization to meet optimal performance criteria such as tractor wheel torque and vehicle speed. The primary objective is to strike a harmonious balance between power delivery and fuel consumption, ensuring seamless adaptation to varying terrains and driving scenarios. By leveraging advanced optimization techniques and utilizing the Jenkins lifetime test cycle, engineers can fine-tune gear ratios to match or surpass the performance of internal combustion engine tractors, all within a two-speed gearbox integrated into the electric tractor.

An essential aspect of this study is the shift from combustion engine tractors, which typically feature a multitude of gear ratios, to electric motors equipped with simplified two-gear transmissions. This transition is made feasible by the electric motor's distinctive ca-

pability to deliver high torques across a broad RPM range. The resulting benefits, reduced complexity in gear selection, and enabling the transmission to navigate rugged terrains and highway conditions effortlessly.

The outcomes of this research significantly contribute to the advancement of transmission design, particularly in agricultural and transportation applications. This study shows an alternative way of gear ratio optimization for tractor transmission technologies. The streamlined and efficient transmission solutions developed through this research not only enhance vehicle performance but also align with sustainability goals, ushering in a new era of innovative and eco-friendly mobility solutions for the agricultural and transportation sectors.

2. Project scope

Agricultural tractors, as typical representatives of off-road vehicles (ORVs), differ from road vehicles in that they have a short working season, long centralized operation time, and heavy working load. Therefore, the power performance and reliability of tractors are the key issues of concern. The power take-off driveline is an important part of a wheeled tractor, which provides rotating power for field machines [7]. As a starting input, internal combustion engine tractor Jenkins cycle is used which shows different tractor speed and corresponding wheel torques for a specific tire option for different gear selection with corresponding time intervals. Jenkins cycle is a unique accelerated bench test which simulates 10 years of lifetime of a tractor. Thus, electric tractor dual mode gearbox needs to deliver almost same or better performance. Here below, it may be seen an example of tractor gearbox bench testing in Figure 1.



Figure 1. Sample gearbox bench testing

For electric tractor dual mode gearbox input from electric motor is crucial and there must be an engine torque/rpm efficiency map to optimize the gear ratios beside tire radius index. Here below in Table 1 summarized sample electric motor inputs.

Table 1. Sample electric motor technical specification.

Engine Max Power (kW)	50
Engine Speed @Max Power (rpm)	3500
Engine Max. Torque (Nm)	180
Engine Speed @Max Torque (rpm)	460
Tire Index Rear (mm)	750

2.1. Dual-mode gearbox ratio inputs

Modern conventional tractors feature intricate gearboxes to provide operators with the widest possible range of working speeds such as up to 24 shifts or more. This complexity is necessary because the rotational speed of the internal combustion engine (ICE) must be appropriately adjusted to meet the specific requirements of each field task, ICE needs to be run at specific range of rpm for its efficiency restrictions [8,9,10]. However, the advent of electric motors has introduced a paradigm shift, leveraging their ability to deliver high torque across a wide RPM range efficiently. This efficiency allows us to achieve the same performance objectives with just two gears, simplifying the transmission system significantly.

In vehicles such as tractors, where wheel torques are very high, a gearbox and axle gears are still required to increase the torques of the electric motor. Alternatively, solutions such as hub motors directly attached to the wheel can be considered. However, this approach has significant disadvantages, especially when working in design-constrained areas, as it tends to be large and very costly. Therefore, a simplified gearbox is highly advantageous due to its low cost and small design volume. Agricultural machinery must be robust enough to endure heavy workloads while remaining cost-effective [11].

The goal is to replicate or even surpass the wheel torque and tractor speeds achieved by internal combustion engine tractors using a dual-mode transmission with two gears—one for road use and the other for field applications. This transition not only enhances performance but also simplifies operation for farmers, eliminating the need for many manual control systems. The critical aspect lies in finding gear ratio optimizations that align with the motor torque RPM efficiency curve—which is shown as a sample in Figure 2, achieved through rigorous testing using the Jenkins cycle for internal combustion engines.

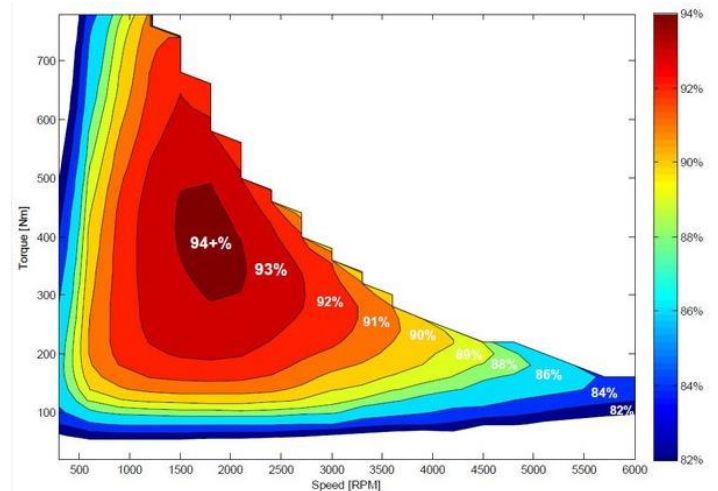


Figure 2. Sample electric motor efficiency map

This study delves into the optimization of gear ratios for dual-mode tractor transmissions, with a focus on the seamless transition from complex combustion engine systems to streamlined electric motor-driven solutions. By leveraging the unique capabilities of electric motors, it is aimed to revolutionize tractor transmission design, making it more efficient, user-friendly, and aligned with modern agricultural practices.

2.2. Jenkins cycle

Tractor driveline should be provided worldwide in the fields of agriculture and construction to different end-users. Therefore, the conditions of application and the loads (e.g. due to soil characteristics) vary considerably from customer to customer [12].

Türk Traktör use a specific cycle to simulate tractor life in the field. The Jenkins cycle is an accelerated powertrain system bench test. Developed through company know-how, this cycle is applied to the powertrain system under test with a specified number of repetitions to ensure that the tractor meets the company's designated lifespan criteria. In this cycle, different gears are simulated with specific durations to mimic the farmer's tractor usage, and the tractor's lifespan is simulated in an accelerated manner with a certain correlation.

During this test, tractor speeds and corresponding wheel torques are applied to the powertrain system at specific time intervals, and it is expected to pass the test. This determines whether the powertrain system's performance under these conditions is suitable and whether tractor can perform the relevant tasks in field conditions without failure. If there is need for improvement, this test is used to identify it.

3. Gear ratio optimization approach

When determining the gear ratios for the 2-speed electric tractor, the approach was centered on achieving performance levels that matched or exceeded those of its equivalent internal combustion engine counterpart. Specifically, it is aimed to ensure that key performance criteria, such as wheel torque and tractor speeds, were either on par with or surpassing those of the internal combustion engine tractor.

For the first gear, designed for field mode and operating within the speed range of 0-16 kph, the objective was to provide wheel torques that were comparable to the internal combustion engine tractor's performance in similar conditions. This was essential to ensure optimal functionality during field operations, where high torque at lower speeds is often required. For the second gear optimized for road mode and operating at speeds below 40 kph. For those 2-gears, the goal was to maintain suitable wheel torques while covering or even exceeding the performance of an equivalent 100 hp internal combustion engine tractor. This required careful consideration of the gear ratios to ensure gearbox robustness, and not inputting much more power that exceeded up to design limit of the complete tractor driveline.

To achieve these objectives, several factors were considered. Firstly, it is implemented a torque limit to ensure that the electric motor's output did not exceed 100 hp. This limit was crucial in maintaining the desired performance levels while preventing excessive strain on the driveline. Additionally, a RPM limit of 7000 RPM was set to avoid overworking the electric motor and to ensure its longevity. This RPM limit was chosen based on the motor's optimal operating range and to prevent any potential overheating or mechanical stress.

The process of determining the optimal gear ratios involved translating the torque and RPM values obtained from the electric motor's performance graph into a comprehensive table. Electric motor matching data points for rpm and torque on the continuous performance curve are a crucial input for gear ratio optimization. This table served as input data for an optimization calculator, which was then used to calculate all tractor speeds and corresponding wheel torques

through various gear cycles. Furthermore, to visualize and compare the performance of the 2-speed gearbox with its internal combustion engine counterpart, graphical representations were created. These visualizations provided valuable insights into how the electric motor's torque and RPM values translated into actual tractor speeds and wheel torques, allowing us to assess whether the selected gear ratios met the performance criteria.

By iteratively refining and testing different gear ratios within the optimization calculator, it may be determined the most suitable gear ratios that not only met but exceeded the performance expectations set by the equivalent internal combustion engine tractor. This meticulous approach ensured that the 2-speed electric tractor could deliver optimal performance across different operating conditions, making it a viable and efficient alternative in agricultural settings. Simple flow chart of the approach summed up as in Figure 3.

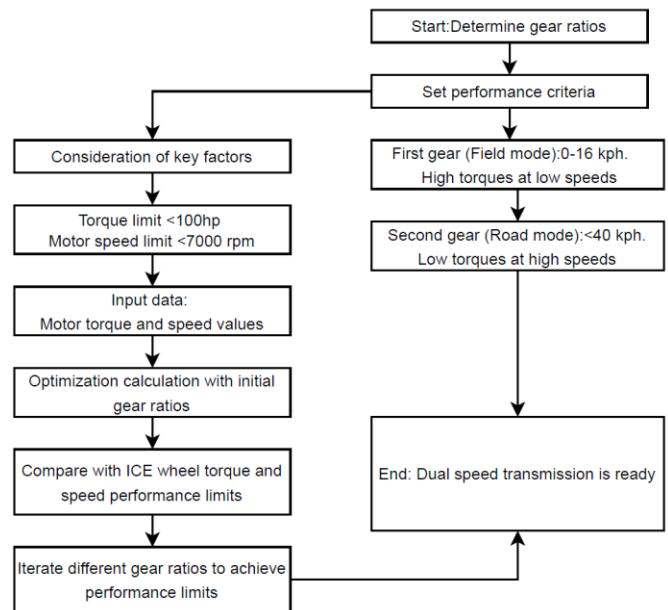


Figure 3. Gear ratio optimization flow chart

4. Gear ratio optimization results

It is delved into the analysis of results derived from the Jenkins cycle data, using the performance metrics of a 100 hp internal combustion engine tractor as the baseline reference for wheel torque and tractor speed data. In Figure 4 it may be found the gear ratio optimization graphics. In the graphics the blue curve represents the wheel torque and tractor speeds observed for the internal combustion engine tractor at the specific gear under examination within the Jenkins cycle. This curve is meticulously constructed by connecting the data points of wheel torque and tractor speeds obtained during the comprehensive testing conducted in the Jenkins cycle.

On the other hand, the green lines depicted in the analysis signify the wheel torque and tractor speeds achieved utilizing the torque and RPM values derived from the electric motor of the tractor. These values are meticulously calculated based on the continuously attained gear ratio. As illustrated in the analysis, the optimized gear ratios culminate in the green lines being consistently positioned above or slightly surpassing the blue curve, signifying an equivalent or slightly enhanced performance compared to the internal combustion engine tractor.

It's imperative to note that each of the two gear ratios serves a distinct purpose within the operational spectrum of the tractor. The first gear, covering tractor speeds ranging from 0-16 kph, is tailored to match or exceed the wheel torques necessary for efficient field operations, aligning with the demands of agricultural tasks. On the other hand, the second gear, designed for speeds between 16-40 kph, is optimized to deliver suitable wheel torques for road usage, ensuring smooth and efficient performance during transportation activities.

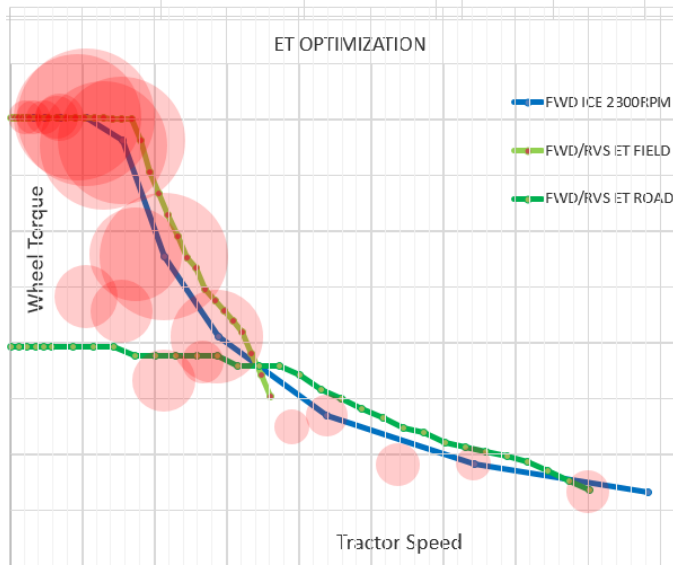


Figure 4. Gear ratio optimization results

Furthermore, the red circles strategically marked in the analysis delineate the specific tractor speeds and corresponding wheel torques where farmers are anticipated to utilize the tractor more frequently. This data not only aids in understanding the operational preferences but also provides crucial insights into the range of operational conditions where this powertrain system will be extensively utilized.

Through this meticulous analysis and data interpretation, it can be derived the optimal gear ratios for the electric tractor, ensuring that its performance matches or exceeds that of its internal combustion engine counterpart across a diverse range of operational scenarios. This detailed analysis serves as the cornerstone for transitioning into the detailed design phase of the gearbox, where all gear pairs will be meticulously designed and calibrated based on the established performance benchmarks.

Indeed, the study yields another significant benefit in terms of analyzing the torque and RPM ranges where the tractor will operate more frequently throughout its entire lifespan, using both the Jenkins cycle data and the determined gear ratios. This analysis allows us to trace backward and visualize the operational patterns of the electric motor, providing valuable insights into the torque and RPM ranges that will be most encountered during its lifetime. In Figure 5 it may found the electric motor torque and rpm usage density.

E-MOTOR DELIVERY ACCORDING TO ICE JENKINS CYCLE

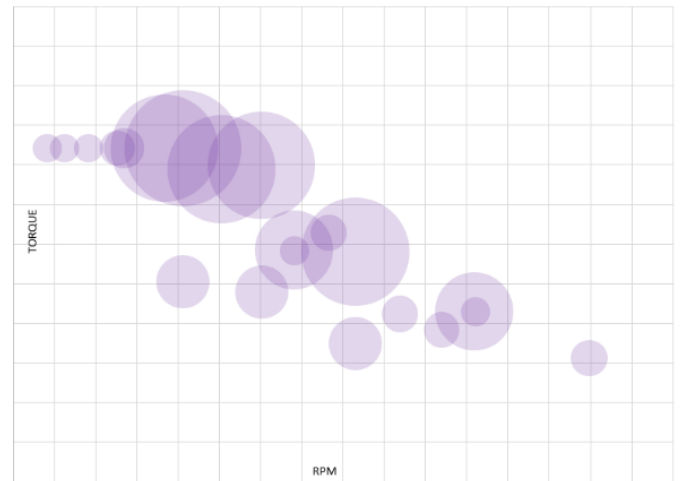


Figure 5. Electric motor torque rpm usage density

This analysis not only aids in optimizing the performance of the tractor but also provides crucial information for motor manufacturers to assess whether their motors can withstand the operational demands anticipated during the tractor's lifespan. By aligning the motor's capabilities with the anticipated torque and RPM requirements, motor manufacturers can ensure the durability and reliability of their motors in real-world agricultural applications.

5. Conclusions

In conclusion, this study focused on optimizing gear ratios for a 2-speed electric tractor, with a particular emphasis on leveraging Jenkins cycle data and analyzing torque and RPM ranges. Through advanced optimization techniques and simulation-based approaches, it is successfully determined gear ratios that matched or exceeded the performance of equivalent internal combustion engine tractors across various operating conditions.

The transition from traditional combustion engines to electric motors presented a paradigm shift which is also force OEMs to find a new way to achieve emissions limits prescribed by the current regulations in force [13,14,15], allowing us to streamline the transmission system with just two gears while maintaining or enhancing performance criteria such as wheel torque and tractor speeds. This transition not only improved efficiency but also simplified operation and reduced complexity for farmers.

Furthermore, the analysis using Jenkins cycle data and backward-looking torque and RPM range analysis provided valuable insights into the tractor's operational dynamics throughout its lifespan. This information is crucial for optimizing tractor performance and ensuring the durability and reliability of electric motors in agricultural applications.

Overall, this research contributes to the advancement of transmission design for electric tractors, making them more efficient, versatile, and suitable for modern agricultural practices. It also underscores the importance of leveraging simulation data and advanced optimization techniques in optimizing gear ratios and enhancing overall tractor performance.

Acknowledgment

This study has been carried out in TürkTraktör R&D Center.

Conflict of Interest Statement

The authors declare that there is no conflict of interest in the study.

CRedit Author Statement

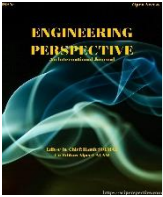
Müjdat Ersarı: Conceptualization Formal analysis, Investigation, Methodology, Writing - original draft

Murat Gündoğdu: Conceptualization, Supervision.







References

- Martelli, S., Mocera, F., & Somà, A. (2023). Carbon footprint of an orchard tractor through a life-cycle assessment approach. *Agriculture*, 13(1210).
- Wollenberg, E., Richards, M., Smith, P., Havlík, P., Obersteiner, M., Tubiello, F. N., Herold, M., Gerber, P., Carter, S., & Reisinger, A. (2016). Reducing emissions from agriculture to meet the 2 °C target. *Global Change Biology*, 22, 3859–3864.
- Golasa, P., Wysokiński, M., Bieńkowska-Golasa, W., Gradziuk, P., Golonko, M., Gradziuk, B., Siedlecka, A., & Gromada, A. (2021). Sources of greenhouse gas emissions in agriculture, with particular emphasis on emissions from energy used. *Energies*, 14(3784).
- Hagan, R., Markey, E., Clancy, J., Keating, M., Donnelly, A., O'Connor, D. J., Morrison, L., & McGillicuddy, E. J. (2023). Non-road mobile machinery emissions and regulations: A review. *Air*, 1, 14–36.
- Lovarelli, D., & Bacenetti, J. (2019). Exhaust gases emissions from agricultural tractors: State of the art and future perspectives for machinery operators. *Biosystems Engineering*, 186, 204–213.
- Bacenetti, J., Lovarelli, D., Facchinetti, D., & Pessina, D. (2018). An environmental comparison of techniques to reduce pollutants emissions related to agricultural tractors. *Biosystems Engineering*, 171, 30–40.
- Kim, W.-S., Kim, Y.-J., Kim, Y.-S., Park, S.-U., Lee, K.-H., Hong, D.-H., & Choi, C.-H. (2021). Evaluation of the fatigue life of a tractor's transmission spiral bevel gear. *Journal of Terramechanics*, 94, 13–22.
- Renius, K. T. (2019). *Fundamentals of tractor design*. Springer: Cham, Switzerland.
- Mattetti, M., Michielan, E., Mantovani, G., & Varani, M. (2022). Objective evaluation of gearshift process of agricultural tractors. *Biosystems Engineering*, 224, 324–335.
- Molari, G., & Sedoni, E. (2008). Experimental evaluation of power losses in a power-shift agricultural tractor transmission. *Biosystems Engineering*, 100, 177–183.
- Pradel, M. (2023). Life cycle inventory data of agricultural tractors. *Data in Brief*, 48, 109174.
- Shin, K., Hwang, J., Kivela, R., Dinner, H., Kwon, Y., & Bae, I. (2007). Tractor transmission verification with KISSsys model.
- European Parliament—Council of the European Union. (2016). Regulation (EU) 2016/1628 of the European Parliament and of the Council of 14 September 2016 on requirements relating to gaseous and particulate pollutant emission limits and type-approval for internal combustion engines for non-road mobile machinery, amending Regulations (EU) No 1024/2012 and (EU) No 167/2013, and amending and repealing Directive 97/68/EC. *Official Journal of the European Union*, 50, 1–76.
- European Parliament Council of the European Union. (2013). Regulation (EU) 167/2013 of the European Parliament and of the Council of

- 5 February 2013 on the approval and market surveillance of agricultural and forestry vehicles.
15. Commission Delegated Regulation (2018) (EU) 2018/985 of 12 February 2018 Supplementing Regulation (EU) No 167/2013 of the European Parliament and of the Council as Regards Environmental and Propulsion Unit Performance Requirements for Agricultural and Forestry Vehicles and Their Engines and Repealing Commission Delegated Regulation (EU) 2015/96.



Fabrication and Characterisation of Sulfonated Polysulfone Membrane with Different Thicknesses for Proton Exchange Membrane Fuel Cell

İrem Tanış^{1*}, Turan Alp Arslan², Tolga Kocakulak^{3,4}, Gülşen Taşkın⁵, Tuğba Tabanlıgil Calam⁵
Hamit Solmaz^{1,6}

¹ Automotive Engineering Department, Faculty of Technology, Gazi University, Ankara, 06500, Turkey

² Automotive Engineering Department, Faculty of Technology, Afyon Kocatepe University, Afyonkarahisar, 03200, Turkey

³ Automotive Engineering Department, Graduate School of Natural and Applied Sciences, Gazi University, Ankara, 06500, Turkey

⁴ Vocational High School of Technical Sciences, Burdur Mehmet Akif Ersoy University, Burdur, 15100, Turkey

⁵ Technical Sciences Vocational High School, Gazi University, Ankara, 06374, Turkey

⁶ Faculty of Engineering, Mechanical Engineering Department, University of Alberta, T6G 1H9, Canada

ABSTRACT

Membranes play a critical role in the performance of proton exchange membrane fuel cells. Membrane thicknesses have positive and negative effects on the characteristics of proton exchange membranes. In this study, sulfonated polysulfone (SPSf) polymer-based membranes with thicknesses of 50 μm , 100 μm , and 150 μm were fabricated, and their characteristic properties were investigated. Water uptake capacity, swelling ratio, proton conductivity, contact angle, chemical stability, and mechanical strength tests were carried out on the membranes. Maximum water uptake capacity and swelling ratio were 45.81% and 13.1% for 100 μm SPSf membrane, respectively. The results of contact angle analysis proved that all synthesized membranes were hydrophilic. Proton conductivity values were measured at different temperatures and solution environments. Significant decreases in resistance values and increases in proton conductivity were observed with decreasing membrane thickness. The increase in temperature and acid in the measurement conditions caused an increase in the proton conductivity value. The highest proton conductivity value was obtained as 0.1971 S/cm in 65 °C and 1 mM hydrochloric acid (HCl) aqueous solution environment in 50 μm SPSf membrane. It was determined that the chemical stability and mechanical strength decreased with the decrease in membrane thickness but remained within the appropriate limits.

Keywords: Fuel Cell; Membrane; Proton Exchange Membrane; Sulfonated Polysulfone; Thickness

History

Received: 09.03.2024

Accepted: 18.07.2024

Author Contacts

*Corresponding Author

e-mail addresses: tanisirem430@gmail.com, talparslan@aku.edu.tr, kocakulak@mehmetakif.edu.tr, gulsentaskin@gazi.edu.tr, ttabanligil@gazi.edu.tr, hsolmaz@gazi.edu.tr

How to cite this paper:

Tanış, İ., Arslan, T.A., Kocakulak, T., Taşkın, G., Calam, T.T., Solmaz, H. (2024). Fabrication and Characterisation of Sulfonated Polysulfone Membrane with Different Thicknesses for Proton Exchange Membrane Fuel Cell. *Engineering Perspective*, 4 (3), 100-107. <http://dx.doi.org/10.29228/eng.pers.77899>

1. Introduction

The world's need for energy is increasing rapidly due to the increase in the human population and the development of industry and technology. This need, which is increasing day by day, has caused wars in the world since the past and adversely affects environmental conditions [1,2]. There is no doubt that fossil fuels such as coal, oil, and natural gas cause environmental pollution, acid rain, global warming, and climate change during energy production. This situation has caused the scientific world to intensify research on alternative and renewable energy sources [3,4].

Renewable energy sources that are environmentally friendly compared to fossil energy sources can be listed as solar, hydroelectric, wind, geothermal, wave, and biomass energy [5-7]. In addition to these energy sources, researches indicate that hydrogen energy is the renewable energy of the future. Since water vapor is released from hydrogen combustion reactions, the environment is not harmed [8]. The technology that uses hydrogen energy most efficiently and economically is fuel cell technology [9].

Fuel cells have advantages such as almost zero emission, easy refueling, noiseless operation, and lightweight. With these advantages,

they can be used in many vehicle types where internal combustion engines and batteries are used. Despite these advantages, they also have disadvantages, such as inefficient storage, transport, and distribution of fuels and high production costs.

Today, fuel cells are classified according to electrolyte type, fuel type, membrane structure material, catalyst material, power density, operating temperature, and efficiency. Fuel cells are divided into six classes according to electrolyte type: alkaline, proton exchange membrane, direct methanol, phosphoric acid, molten carbonate, and solid oxide fuel cells [10-12]. Proton exchange membrane fuel cell (PEMFC) has primary advantages over other fuel types, such as no risk of electrolyte leakage, short warm-up time, and high specific power. Therefore, the PEM fuel cell is one of the most preferred fuel cells today [13,14]. Proton exchange membrane (PEM) fuel cell is a type of fuel cell that directly and efficiently converts the chemical energy stored in the fuel into electrical energy, providing high power and energy at low operating temperatures.

Fuel cells consist of gas flow plate, gas diffusion layer, catalyst layer, membrane, current collector plate, and sealing components [15]. The gas flow plate ensures that the fluids in the fuel cell are evenly and effectively distributed on the electrode surface. It also helps to remove the heat generated during electrochemical reactions from the cell. The gas diffusion layer ensures that hydrogen and oxygen gases are evenly and continuously delivered to the catalyst layer. In addition to this task, it helps to transmit the electricity generated in the catalyst to the gas flow plate and from there to the external circuit. In the cell, the catalyst layer is where reduction and oxidation reactions occur. It separates and combines reactive gases (hydrogen and oxygen). Membranes transmit protons formed by the breakdown of hydrogen on the anode side to the cathode side. Since it is not permeable to electrons, it causes electrons to flow through the external circuit and produces electrical energy [16,17].

In order to expand the usage area of fuel cells further, cost, efficiency, and performance values should be improved. For this reason, researchers have conducted various studies to determine the effects of thickness variation of the membrane, which is one of the critical components of the fuel cell. For example, Lufrano et al. synthesized membranes with different sulfonation degrees (57% and 66%) and thicknesses (70, 120, and 150 μm) for direct methanol fuel cell (DMFC) and characterized them in terms of methanol/water uptake, proton conductivity, and fuel cell performances at room temperature in passive mode. They obtained the best performance with 70 μm SPSf-2 membrane (66% sulfonation degree) [18]. Zhang et al. synthesized SPSf membranes with various sulfonation degrees (62%, 67%, 76%, and 91%) and thicknesses (76, 80, 79, and 76 μm). They characterized the physicochemical properties, ion permeability, and vanadium redox flow battery (VRFB) performance of the obtained SPSf membranes. As a result of the study, the SPSf-62 membrane with 62% sulfonation degree showed the best performance. This membrane exhibited better ion permeability and cycle stability than Nafion 117 [19]. Zhao et al. studied the effect of Nafion (117, 115, and 112) thickness on DMFC. With Nafion 117, 115, and 112 membranes with thicknesses of 174, 125, and 50 μm , they found that a thicker membrane showed higher fuel efficiency. However, the fuel cell performance varied with different operating conditions, such as methanol concentration and current density [20].

As a result of the literature search, there is quite a limited number

of studies investigating the effect of thickness on the characteristic properties of SPSf-based polymer membranes produced for use in PEM fuel cells. For this reason, in this study, SPSf membranes with thicknesses of 50 μm , 100 μm , and 150 μm were produced and characterized for proton exchange membrane fuel cells. During the characterization process, water uptake capacity, swelling ratio, proton conductivity, contact angle, chemical stability, and mechanical strength tests were carried out, and the effects of thickness on membrane performance were investigated.

2. Materials and Methods

In this study, fabrication and characterization of SPSf polymer-based PEM fuel cell membranes with 50 μm , 100 μm , and 150 μm thicknesses were carried out. Water uptake capacity, swelling ratio, proton conductivity, contact angle, chemical stability, and mechanical strength tests were applied to the fabricated membranes. As a result of the characterization processes, the physical, chemical, and electrochemical performances of membranes with different thicknesses were investigated.

2.1. Sulfonation process

Pure polysulfone (PSf) pellets (Sigma-Aldrich), chloroform (Sigma-Aldrich), and sulfuric acid (H_2SO_4 , Merck) were used for the sulfonation of PSf polymer. Firstly, 10 g PSf was weighed and dissolved in 100 ml chloroform with the help of a magnetic stirrer. The sulfonation process was started by slowly adding 3 ml H_2SO_4 to the stirring solution. The stirring process was continued for 6 hours, which is the sulfonation duration. In order to complete the sulfonation, the prepared solution was transferred to an ice water bath, and the polymers were precipitated [21]. The precipitated polymers were washed with distilled water until neutralized. Ohaus brand AB23PH-F model digital pH meter was used to measure the pH value of the solution. After washing, SPSf polymers were dried in an oven at 80 $^\circ\text{C}$ for 48 hours [22].

2.2. Synthesis of membranes

In the study, membranes with thicknesses of 50 μm , 100 μm , and 150 μm were produced. For each membrane sample, 2 g of SPSf polymer was weighed using a precision balance. After weighing, SPSf was dissolved with 5 mL dichloromethane (DCM, Aklar Kimya). Membrane castings were carried out using the Biuged Instruments brand BGD-219 model automatic film applicator. SPSf membranes of the specified thicknesses were left to dry at room temperature after casting. Images of the membrane samples are shown in Figure 1.

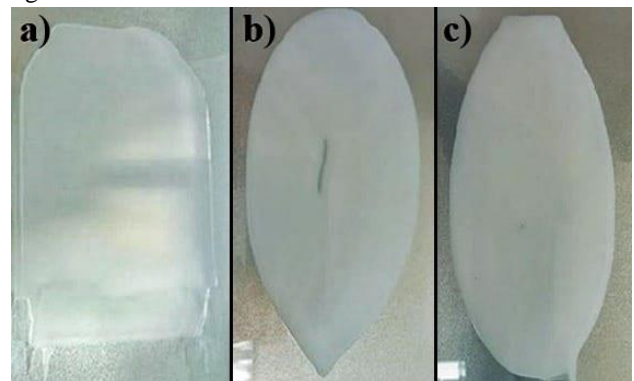


Figure 1. SPSf membrane samples: a) 50 μm , b) 100 μm , and c) 150 μm

2.3. Water uptake capacity and swelling ratio analyses

Water uptake capacity is the most important of the properties affecting proton conductivity in membranes. Membranes with high water uptake capacity are needed for high proton conductivity values [23]. However, with the increase in water uptake capacity, an increase in the swelling properties of membranes can also be observed. With swelling, the membrane thickness increases and creates proton conduction resistance [24]. Therefore, it is desired to keep the membrane water uptake at an optimum level [25]. Membrane water uptake capacity and swelling ratio values can be determined by experimental methods.

To determine water uptake capacity (WU) and swelling ratio (SR), SPSf membrane samples were dried in an oven at 70 °C for 24 h. Mass and dimensional measurements of the dried membrane samples were made. Afterwards, the membranes were kept in deionized water for 24 h. After the membranes were dewatered, the mass and dimensional measurements of the samples were carried out again. Using the measured masses and dimensions of dry and wet membranes, the water uptake capacity was calculated by Eq. (1), and the swelling ratio was calculated by Eq. (2) [26,27].

$$WU (\%) = \frac{m_{wet} - m_{dry}}{m_{dry}} \cdot 100 \quad (1)$$

$$SR (\%) = \frac{V_{wet} - V_{dry}}{V_{dry}} \cdot 100 \quad (2)$$

Where m_{wet} is wet mass, m_{dry} is dry mass, V_{wet} is wet volume and V_{dry} is dry volume.

2.4. Measurement of proton conductivity

Proton conductivity (σ) is the most important criterion for the performance and efficiency of proton exchange membrane fuel cells. In order to increase the proton conductivity in proton exchange membrane fuel cells, the membrane resistance should be low as well as the appropriate operating temperature and humidity [28]. The proton conductivity of membranes can be measured using the Electrochemical Impedance Spectroscopy (EIS) technique with the help of 2, 3, or 4 probe cells and potentiostat [29-31]. The 4-probe measurement method is widely preferred thanks to its better measurement accuracy [32].

In this study, proton conductivities were measured in two different environments. The first was deionized water at 25 °C; the second was 1 mM hydrochloric acid (HCl) and aqueous solution at 65 °C. The proton conductivity measurement process and the measurement cell with four probes are shown in Figure 2.

Ivium brand Compartment model electrochemical workstation was used in the measurements. The measurements were performed at a frequency range of 1 Hz-100 kHz, and an amplitude of 0.1 V. IviumSoft software was used to create equivalent electrical circuit models of SPSf membranes and to determine the resistance values. Proton conductivities of the membranes were calculated with Eq. (3) by utilizing the measured membrane resistance and sample dimensions [33].

$$\sigma = \frac{L}{R \cdot w \cdot t} \quad (3)$$

Where L is the distance between the two internal electrodes, R is

the membrane resistance, w is the membrane width, and t is the membrane thickness.

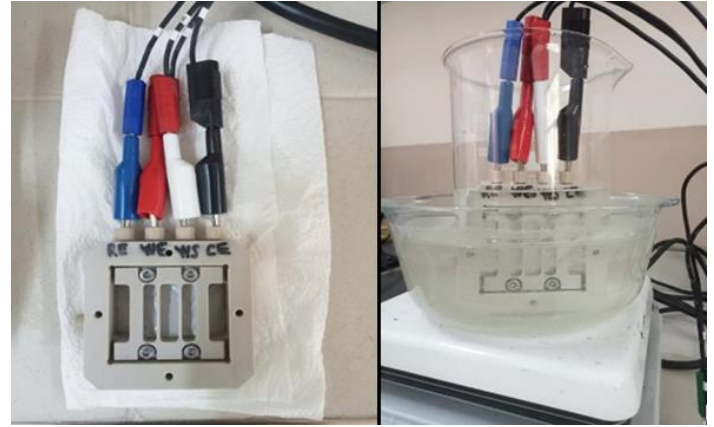


Figure 2. Four-probe cell and measurement process

2.5. Contact angle analysis

Wetting is defined as the ability of the liquid to maintain the contact of the liquid on the solid due to the effect of adhesion forces at the solid-liquid interface during the contact of liquid and solid surfaces. The indicator of the wettability of a solid object with a liquid is the contact angle between the liquid drop and the solid surface [34]. The contact angle can vary between 0° and 180°. A contact angle smaller than 90° means the material is hydrophilic, and a larger contact angle means the material is hydrophobic [35]. Contact angle analyses are performed to evaluate membranes' hydrophilic and hydrophobic characteristics [36].

Contact angles of SPSf membranes of different thicknesses were measured at room temperature using the sessile drop method and deionized water. Biolin Scientific brand Attension Theta model optical contact angle measuring device was used in the measurements.

2.6. Fenton chemical stability test

The degradation of proton exchange membranes is caused by chemical, electrochemical, mechanical, and thermal reasons. Degradation of PEMs can significantly reduce fuel cell efficiency [37,38]. The Fenton test is widely preferred for investigating the chemical stability of PEM fuel cell membranes [39].

To determine the chemical stability of SPSf membranes, a Fenton reagent solution was prepared using iron II sulfate (FeSO_4 , Aklar Kimya), hydrogen peroxide (50%, H_2O_2 , Aklar Kimya), and deionized water. In the first stage of the Fenton test, membranes of different thicknesses were kept in an oven at 70°C for 24 hours and weighed. Then, the dry membranes were kept in 3% H_2O_2 , 4 ppm Fe^{+2} aqueous solution for 1 day and 7 days. At the end of this period, the membranes were dried again in the oven under the same conditions, and their final masses were recorded. The weight loss (WL) resulting from the Fenton reaction was calculated by Eq. (4) using the measured masses of the membranes.

$$WL (\%) = \frac{m_{initial} - m_{end}}{m_{initial}} \cdot 100 \quad (4)$$

Where $m_{initial}$ is the initial weight of the membranes after drying and m_{end} is the final weight after the Fenton reaction.

2.7. Mechanical strength test

The membrane can be defined as the backbone of the membrane-electrode assembly [40]. Mechanical strength tests are aimed to determine Young's modulus, tensile stress, and elongation at break values of membranes.

TIRA Test brand 2710 model tensile tester was used in mechanical strength tests of SPSf membranes. For mechanical strength tests, membranes of different thicknesses were cut to the specific dimensions, and tensile tests were carried out at room temperature at 2 mm/min speed. Elongation (ϵ), elongation at break (EB), Young's modulus (E), and tensile strength (σ_t) values were calculated by Eq. (5), Eq. (6), Eq. (7), and Eq. (8), respectively.

$$\epsilon = \frac{\Delta L}{L} \quad (5)$$

$$EB (\%) = \frac{\Delta L}{L} \cdot 100 \quad (6)$$

$$E = \frac{\sigma}{\epsilon} \quad (7)$$

$$\sigma_t = \frac{F_{max}}{A_i} \quad (8)$$

In the equations, ΔL is the change in the sample length, L is the initial length of the sample, F_{max} is the maximum tensile force applied to the sample, and A_i is the initial cross-sectional area of the sample.

3. Results and Discussions

In the study, the water uptake capacity, swelling ratio, proton conductivity, weight loss as a result of the Fenton reaction, tensile stress, Young's modulus, and elongation at break values of SPSf polymer-based proton exchange membranes with different thicknesses were characterized, and the effects of changes in thickness on membrane performance were investigated.

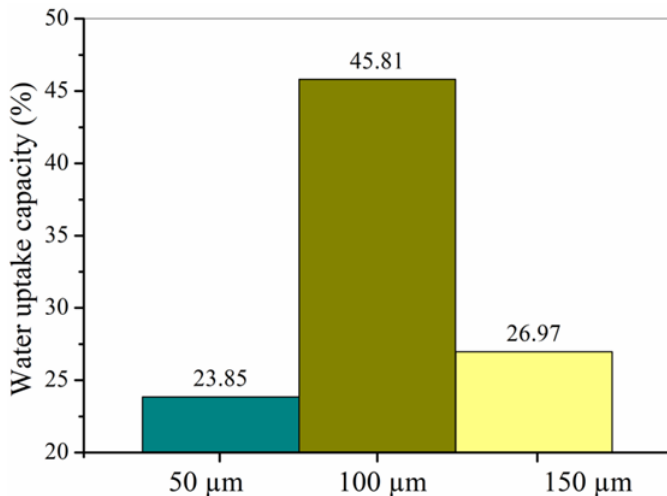


Figure 3. Water uptake capacity of SPSf membranes

3.1. Water uptake capacity

Water uptake capacity is one of the most critical parameters that trigger the proton conductivity of PEM fuel cell membranes. The water uptake properties of PEMs may vary depending on their thickness. The water uptake capacity values of the synthesized SPSf

membranes are shown in Figure 3. The water uptake capacities of the membranes with 50 μm , 100 μm , and 150 μm thicknesses were determined as 23.85%, 45.81%, and 26.97%, respectively. The highest water uptake capacity value was obtained in the membrane with 100 μm thickness.

3.2. Swelling ratio

It is desired that the membranes have a high water uptake capacity but a low swelling ratio. The reason for this is that the stresses due to swelling negatively affect the mechanical strength of the membrane, and the increase in thickness makes proton conductivity difficult. Swelling ratios for SPSf membranes with different thicknesses are presented in Figure 4. The swelling ratios for membranes with 50 μm , 100 μm , and 150 μm thicknesses were obtained as 4.6%, 13.1%, and 3.5%, respectively. The high water uptake capacity in the 100 μm membrane resulted in a high swelling ratio.

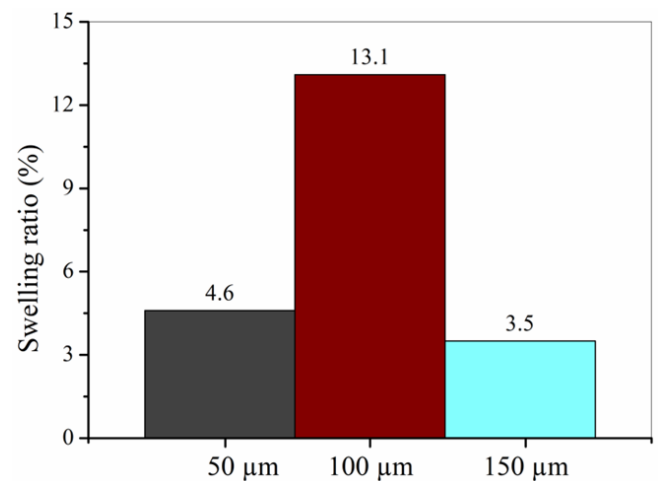


Figure 4. Swelling ratio of SPSf membranes

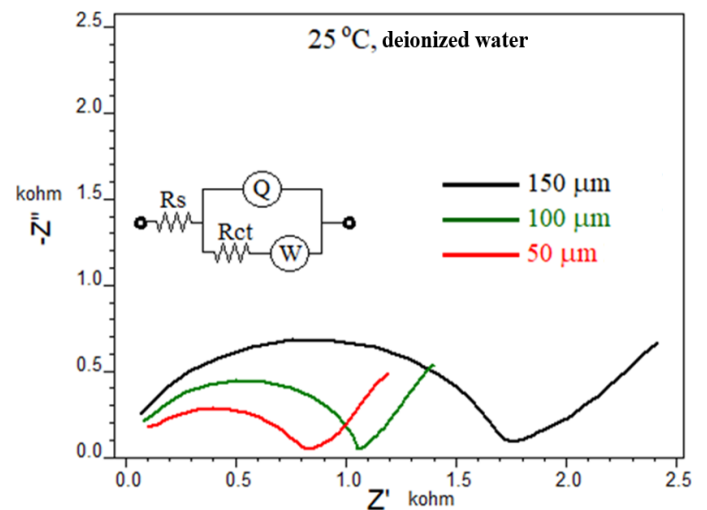


Figure 5. Nyquist plots of SPSf membranes (25 °C and deionized water)

3.3. Proton conductivity

Proton conductivity is one of the most important characteristics of PEM fuel cells. Membrane resistance directly affects proton conductivity. The Nyquist plot of membranes with different thicknesses at 25 °C and in deionized water environment is shown in Figure 5. A

significant increase in resistance values occurred with the increase in the thickness of SPSf membranes.

The Nyquist graph of SPSf membranes created at 65 °C temperature and 1 mM HCl aqueous solution environment is shown in Figure 6. Similar to the deionized water environment, a regular decrease in the resistance value occurred here as the membrane thickness decreased. At the same time, thanks to the increasing temperature and acid environment, the resistance values resulted in a lower level than those of the deionized water environment.

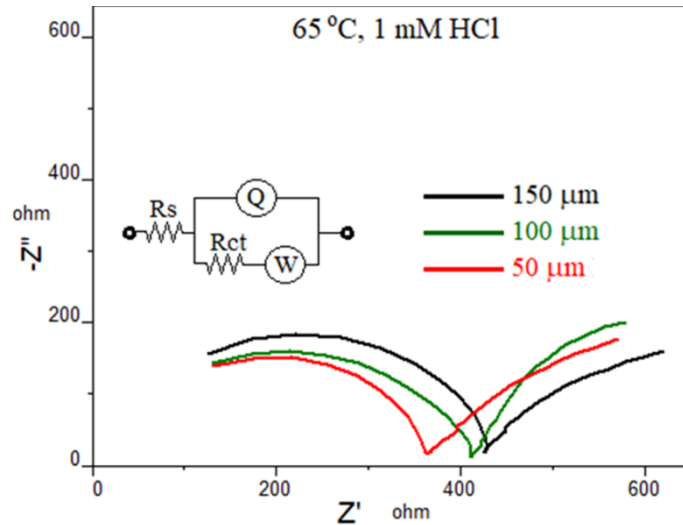


Figure 6. Nyquist plots of SPSf membranes (65 °C and 1 mM HCl)

The resistance values obtained in different measurement environments of SPSf membranes with different thicknesses are shown in Table 1, and the proton conductivity results calculated with these resistance values and dimensional parameters are shown in Table 2.

Table 1. Resistance values of SPSf membranes

Measurement conditions	Units	Membrane thickness (μm)		
	μm	50	100	150
25 °C, deionized water	kohm	798.9	1038	172.5
65 °C, 1 mM HCl	kohm	277.6	313.4	396

Table 2. Proton conductivity values of SPSf membranes

Measurement conditions	Units	Membrane thickness (μm)		
	μm	50	100	150
25 °C, deionized water	S/cm	0.0684	0.0205	0.0108
65 °C, 1 mM HCl	S/cm	0.1971	0.0613	0.0472

When the obtained results were examined, the highest proton conductivity in both environments was in the 50 μm SPSf membrane, while the lowest proton conductivity was in the 150 μm membrane. As the thickness of the SPSf membrane increased, a decrease in proton conductivity was observed. SPSf membranes showed higher proton conductivity in 65 °C, 1 mM HCl aqueous solution. One reason is that high temperature increases the activation energy and enables faster movement of protons. The second reason is that HCl opens proton carrier paths in the membrane [41]. As a result of impedance analysis, the highest proton conductivity value was measured as 0.1971

S/cm in 50 μm SPSf membrane in 65 °C and 1 mM HCl aqueous solution environment.

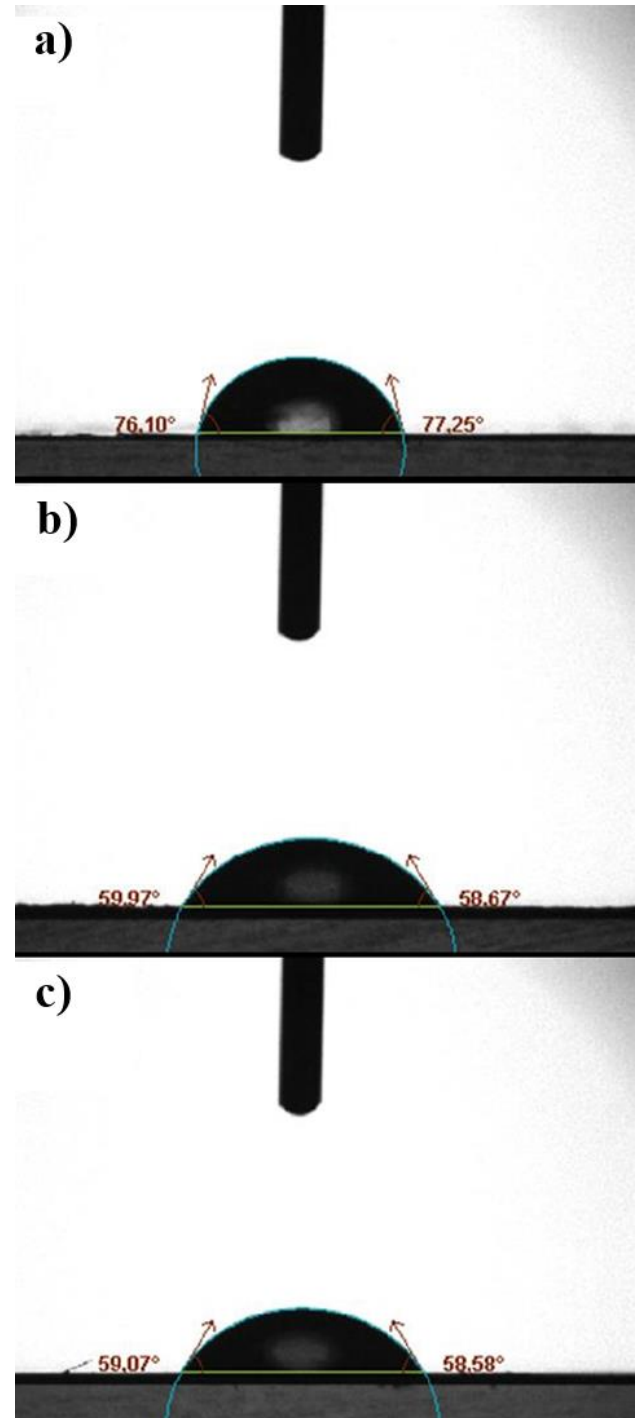


Figure 7. Contact angle images of SPSf membranes

3.4. Contact angle

Contact angle analyses were performed to evaluate the hydrophilic and hydrophobic characteristics of SPSf membranes produced with different thicknesses. Contact angle images of SPSf membranes are shown in Figure 7, and the average values of contact angle measurements are shown in Figure 8. The average contact angle values of SPSf membranes with thicknesses of 50 μm, 100 μm, and 150 μm were measured as 76.67°, 59.32°, and 58.83°, respectively. After the

analysis, it was concluded that all synthesized membranes were hydrophilic.

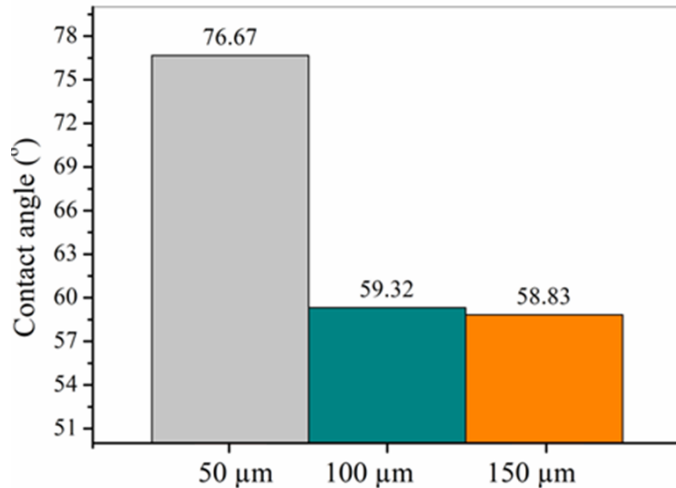


Figure 8. Contact angles of SPSf membranes

3.5. Fenton chemical stability

The Fenton test is used to evaluate chemical degradation caused by hydroxyl radicals and its effects on fuel cell performance. The weight losses resulting from the Fenton reaction of membranes with thicknesses of 50 μm, 100 μm, and 150 μm are shown in Figure 9. When the results after 24 hours are examined, it is seen that the lowest weight loss was obtained as 4.42% in the membrane with a thickness of 100 μm. The highest weight loss occurred as 23.03% in the membrane with a thickness of 50 μm after 168 hours.

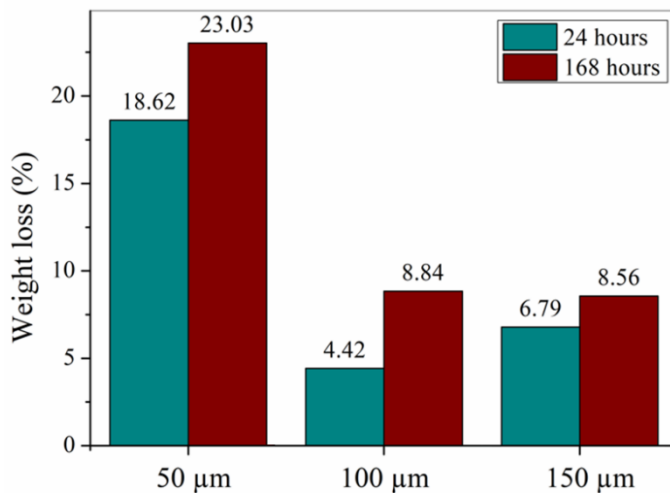


Figure 9. Fenton weight loss of SPSf membranes

3.6. Mechanical strength

The mechanical strength of the membranes is of critical importance for the performance, efficiency, and life of the fuel cell [42]. The values of elongation at break, Young's modulus, and tensile strength obtained by applying tensile tests for SPSf membranes with different thicknesses are presented in Table 3. The highest tensile stress value was 21.2 Mpa for the 100 μm membrane. The highest Young's modulus value was 764.7 Mpa for the 150 μm membrane. The elongation at break values of the membranes with thicknesses

of 50 μm, 100 μm, and 150 μm were 8.9%, 6.42%, and 5.54%, respectively. A regular decrease was observed in the elongation at break values with increasing thickness.

Table 3. Mechanical strength results of SPSf membranes

Samples	Tensile strength (MPa)	Young modulus (MPa)	Elongation at break (%)
50 μm	19.2	751.48	8.9
100 μm	21.2	713.44	6.42
150 μm	19.2	764.7	5.54

4. Conclusions

In this study, SPSf polymer-based membranes with 50 μm, 100 μm, and 150 μm thickness were fabricated, and their characteristic properties were investigated. The highest water uptake capacity and swelling ratio were obtained as 45.81% and 13.1% for 100 μm membranes, respectively. It was observed that the resistance value decreased with decreasing membrane thickness, and proton conductivity increased. The increase in temperature and acid in the measurement environment caused an increase in the proton conductivity value. The highest proton conductivity value was obtained as 0.1971 S/cm in 50 μm SPSf membrane at 65 °C and 1 mM HCl aqueous solution. As a result of contact angle analyses, it was observed that SPSf membranes of all thicknesses synthesized were hydrophilic. Chemical stability was positively affected by the increase in membrane thickness. The highest tensile strength value was obtained as 21.2 Mpa in the membrane with a thickness of 100 μm. A regular increase in elongation at break was observed with the decrease in membrane thickness.

Acknowledgment

This study was supported by Gazi University Research Projects Coordination Unit (BAP) with project number of FGA-2023-7912 in the scope of Research Universities Support Program.

Conflict of Interest Statement

The authors declare that there is no conflict of interest in the study.

CRedit Author Statement

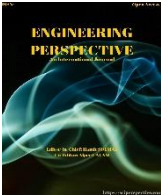
İrem Tanış: Writing-original draft, Visualization, Investigation, Conceptualization. **Turan Alp Arslan:** Writing-original draft, Visualization, Investigation. **Tolga Kocakulak:** Writing-original draft, Visualization, Investigation. **Gülşen Taşkın:** Writing – review & editing, Investigation, Methodology. **Tuğba Tabanlıgil Calam:** Writing – review & editing, Investigation, Conceptualization. **Hamit Solmaz:** Writing – review & editing, Supervision, Project administration, Methodology.

References

- Deshmukh, M. K. G., Sameeroddin, M., Abdul, D., & Sattar, M. A. (2023). Renewable energy in the 21st century: A review. *Materials Today: Proceedings*, 80, 1756-1759.
- Xu, Y., & Zhao, F. (2023). Impact of energy depletion, human development, and income distribution on natural resource sustainability. *Resources Policy*, 83, 103531.
- Kocakulak, T., & Arslan, T. A. (2023). Investigation of the use of fuel cell hybrid systems for different purposes. *Engineering Perspective*, 3(1), 1-8.

4. Majeed, Y., Khan, M. U., Waseem, M., Zahid, U., Mahmood, F., Majeed, F., ... & Raza, A. (2023). Renewable energy as an alternative source for energy management in agriculture. *Energy Reports*, 10, 344-359.
5. Zahedi, R., Sadeghitabar, E., Khazaei, M., Faryadras, R., & Ahmadi, A. (2024). Potentiometry of wind, solar and geothermal energy resources and their future perspectives in Iran. *Environment, Development and Sustainability*, 1-27.
6. Awad, M., Said, A., Saad, M. H., Farouk, A., Mahmoud, M. M., Alshammari, M. S., ... & Omar, A. I. (2024). A review of water electrolysis for green hydrogen generation considering PV/wind/hybrid/hydropower/geothermal/tidal and wave/biogas energy systems, economic analysis, and its application. *Alexandria Engineering Journal*, 87, 213-239.
7. Aniakor, C. O. (2024). Mapping renewable energy technologies (solar, wind and geothermal) to the United Nations' Sustainable Development Goals (SDGs) to reveal and quantify synergies and tradeoffs. Available at SSRN: 10.2139/ssrn.4842618.
8. Van Der Linden, F., Pahon, E., Morando, S., & Bouquain, D. (2023). A review on the proton-exchange membrane fuel cell break-in physical principles, activation procedures, and characterization methods. *Journal of Power Sources*, 575, 233168.
9. Bodkhe, R. G., Shrivastava, R. L., Soni, V. K., & Chadge, R. B. (2023). A review of renewable hydrogen generation and proton exchange membrane fuel cell technology for sustainable energy development. *International Journal of Electrochemical Science*, 18(5), 100108.
10. Kumuk, B. (2019). A review of fuel cell types and applications. *Turkish Journal of Energy Policy*, 4(9), 1-9.
11. Ramasamy, P., Muruganantham, B., Rajasekaran, S., Babu, B. D., Ramkumar, R., Marthanda, A. V. A., & Mohan, S. (2024). A comprehensive review on different types of fuel cell and its applications. *Bulletin of Electrical Engineering and Informatics*, 13(2), 774-780.
12. Shuhayeu, P., Martsinchyk, A., Martsinchyk, K., Szczeńniak, A., Szablowski, Ł., Dybiński, O., & Milewski, J. (2024). Model-based quantitative characterization of anode microstructure and its effect on the performance of molten carbonate fuel cell. *International Journal of Hydrogen Energy*, 52, 902-915.
13. Mancino, A. N., Menale, C., Vellucci, F., Pasquali, M., & Bubbico, R. PEM fuel cell applications in road transport. *Energies*, 16(17), 6129.
14. Maher, A. R., & Sadiq, A. B. (2013). PEM fuel cells: Fundamentals, modeling, and applications. Create Space Independent Publishing Platform, Washington.
15. Amani, B., & Zanj, A. (2023). Analysis of the effects of the gas diffusion layer properties on the effectiveness of baffled flow channels in improving proton exchange membrane fuel cells performance. *International Communications in Heat and Mass Transfer*, 140, 106558.
16. Zhou, S., Xie, G., Hu, H., & Ni, M. (2023). Simulation on water transportation in gas diffusion layer of a PEM fuel cell: Influence of non-uniform PTFE distribution. *International Journal of Hydrogen Energy*, 48(28), 10644-10658.
17. Zhang, G., Qu, Z., & Wang, Y. (2023). Proton exchange membrane fuel cell of integrated porous bipolar plate-gas diffusion layer structure: Entire morphology simulation. *eTransportation*, 17, 100250.
18. Lufano, F., Baglio, V., Staiti, P., Stassi, A., Aricò, A. S., & Antonucci, V. (2010). Investigation of sulfonated polysulfone membranes as electrolyte in a passive-mode direct methanol fuel cell mini-stack. *Journal of Power Sources*, 195(23), 7727-7733.
19. Zhang, Y., Zheng, L., Liu, B., Wang, H., & Shi, H. (2019). Sulfonated polysulfone proton exchange membrane influenced by a varied sulfonation degree for vanadium redox flow battery. *Journal of Membrane Science*, 584, 173-180.
20. Liu, J. G., Zhao, T. S., Liang, Z. X., & Chen, R. (2006). Effect of membrane thickness on the performance and efficiency of passive direct methanol fuel cells. *Journal of Power Sources*, 153(1), 61-67.
21. Kocakulak, T., Taşkın, G., Calam, T. T., Solmaz, H., Calam, A., Arslan, T. A., & Şahin, F. (2024). A new nanocomposite membrane based on sulfonated polysulfone boron nitride for proton exchange membrane fuel cells: Its fabrication and characterization. *Fuel*, 374, 132476.
22. Lufano, F., Gatto, I., Staiti, P., Antonucci, V., & Passalacqua, E. (2001). Sulfonated polysulfone ionomer membranes for fuel cells. *Solid State Ionics*, 145(1-4), 47-51.
23. Wang, G., Kang, J., Yang, S., Lu, M., & Wei, H. (2024). Influence of structure construction on water uptake, swelling, and oxidation stability of proton exchange membranes. *International Journal of Hydrogen Energy*, 50, 279-311.
24. Selim, A., Szijjártó, G. P., Románszki, L., & Tompos, A. (2022). Development of WO₃-Nafion based membranes for enabling higher water retention at low humidity and enhancing PEMFC performance at intermediate temperature operation. *Polymers*. 14(12), 2492.
25. Chen, F., Dong, W., Lin, F., Ren, W., & Ma, X. (2021). Composite proton exchange membrane with balanced proton conductivity and swelling ratio improved by gradient-distributed POSS nanospheres. *Composites Communications*, 24, 100676.
26. Li, J., Cui, N., Liu, D., Zhao, Z., Yang, F., Zhong, J., & Pang, J. (2024). SPEEK-co-PEK-x proton exchange membranes with controllable sulfonation degree for proton exchange membrane fuel cells. *International Journal of Hydrogen Energy*, 50, 606-617.
27. Zhang, Y., Zhang, A., He, H., Fan, Y., Li, Y., Wang, S., & Li, S. (2024). Fabrication of an ultra-thin and ordered SPEEK proton exchange membrane by a Langmuir-Blodgett self-assembly process. *Journal of Membrane Science*, 690, 122196.
28. Peighambari, S. J., Rowshanzamir, S., & Amjadi, M. (2010). Review of the proton exchange membranes for fuel cell applications. *International Journal of Hydrogen Energy*, 35(17), 9349-9384.
29. Lvovich, V. F. (2012). Impedance spectroscopy: Applications to electrochemical and dielectric phenomena. John Wiley & Sons.
30. Karpenko, L. V., Demina, O. A., Dvorkina, G. A., Parshikov, S. B., Larchet, C., Auclair, B., & Berezina, N. P. (2001). Comparative study of methods used for the determination of electroconductivity of ion-exchange membranes. *Russian Journal of Electrochemistry*, 37(3), 287-293.
31. Sistat, P., Kozmai, A., Pismenskaya, N., Larchet, C., Pourcelly, G., & Nikonenko, V. (2008). Low-frequency impedance of an ion-exchange membrane system. *Electrochimica Acta*, 53(22), 6380-6390.
32. Zhang, Y., Zhu, C., Zhang, J., & Liu, Y. (2024). Negative impact of poly(acrylic acid) on proton conductivity of electrospun catalyst layers. *Applied Energy*, 357, 122511.
33. Ng, W. W., San Thiam, H., Pang, Y. L., Lim, Y. S., Wong, J., & Saw, L. H. (2023). Self-sustainable, self-healable sulfonated graphene oxide incorporated nafion/poly(vinyl alcohol) proton exchange membrane for direct methanol fuel cell applications. *Journal of Environmental Chemical Engineering*, 11(6), 111151.
34. Bormashenko, E. Y. (2013). Wetting of real surfaces. Walter de Gruyter GmbH, Berlin.

35. Cosgrove, T. (2005). *Colloid science (Principles, methods and applications)*. Wiley-Blackwell Publishing Ltd., Oxford.
36. Sigwadi, R., Dhlamini, M. S., Mokrani, T., & Nemavhola, F. (2019). Enhancing the mechanical properties of zirconia/Nafion® nanocomposite membrane through carbon nanotubes for fuel cell application. *Helvion*, 5(7), e02112.
37. Inaba, M., Kinumoto, T., Kiriake, M., Umebayashi, R., Tasaka, A., & Ogumi, Z. (2006). Gas crossover and membrane degradation in polymer electrolyte fuel cells. *Electrochimica Acta*, 51(26), 5746-5753.
38. Cheng, X., Zhang, J., Tang, Y., Song, C., Shen, J., Song, D., & Zhang, J. (2007). Hydrogen crossover in high-temperature PEM fuel cells. *Journal of Power Sources*, 167(1), 25-31.
39. Oh, S., Kim, J., Lee, D., & Park, K. (2018). Variation of hydrogen peroxide concentration during fenton reaction for test the membrane durability of PEMFC. *Korean Chemical Engineering Research*, 56(3), 315-319.
40. Dafalla, A. M., & Jiang, F. (2018). Stresses and their impacts on proton exchange membrane fuel cells: A review. *International Journal of Hydrogen Energy*, 43(4), 2327-2348.
41. Liu, W., Luo, N., Li, P., Yang, X., Dai, Z., Song, S., ... & Zhang, H. (2020). New sulfonated poly(ether ether ketone) composite membrane with the spherical bell-typed superabsorbent microspheres: Excellent proton conductivity and water retention properties at low humidity. *Journal of Power Sources*, 452, 227823.
42. Wallnöfer-Ogris, E., Poimer, F., Köll, R., Macherhammer, M. G., & Trattner, A. (2024). Main degradation mechanisms of polymer electrolyte membrane fuel cell stacks—Mechanisms, influencing factors, consequences, and mitigation strategies. *International Journal of Hydrogen Energy*, 50, 1159-1182.



Modeling and simulation of an Internal Combustion Engine using Hydrogen: A MATLAB implementation approach

Quang Truc Dam^{1,*} , Fatima Haidar¹ , Nour Mama¹ , Sherwin Joy Chennapalli¹ 

¹ Capgemini Engineering, Research & Innovation Direction, 12 rue de la Verrerie, 92190, Meudon, France

ABSTRACT

In response to the escalating global demand for energy spurred by industrialization, nations are increasingly turning to alternative fuel sources. Among these alternatives, hydrogen stands out for its remarkable efficiency and environmental benefits. With its potential to significantly reduce fuel consumption and air pollution, particularly in the transportation sector, hydrogen has garnered widespread attention as a promising solution to our energy challenges. This study focuses on the development of a dynamic model for an internal combustion engine powered by hydrogen (H₂-ICE). By intricately dissecting and modeling the various components of the engine and their interactions, we aim to create a comprehensive simulation platform. This platform will enable us to accurately predict and analyze the performance of H₂-ICE under different operating conditions. Through the utilization of advanced simulation tools like Matlab Simulink, we can validate the efficacy and reliability of our model, providing valuable insights into the behaviour of hydrogen-powered engines. Furthermore, the implications of this research extend beyond mere simulation. The developed model opens up avenues for further exploration and innovation in the field of hydrogen propulsion. For instance, it lays the groundwork for the development of sophisticated control systems tailored specifically for H₂-ICE applications. Additionally, the effectiveness of the proposed model in terms of air intake dynamics, pressure, temperature, fuel injection response, combustion efficiency, and overall engine performance, such as power output, torque, and engine velocity are illustrated through simulation results using Matlab Simulink.

Keywords: Automotive, Engine, Hydrogen, MATLAB - Simulink

History

Received: 04.03.2024

Accepted: 23.07.2024

Author Contacts

*Corresponding Author

e-mail addresses : Quang-truc.dam@capgemini.com , Fatima.haidar@capgemini.com ,

Nour.mama@capgemini.com , Sherwin-joy.chennapalli@capgemini.com

How to cite this paper:

Dam, Q.T., Haidar, F., Mama, N., Chennapalli, S.J., (2024). Modeling and simulation of an Internal Combustion Engine using Hydrogen: A MATLAB implementation approach. Engineering Perspective, 4 (3), 108-118. <http://dx.doi.org/10.29228/eng.pers.76219>

1. Introduction

With the increase in the global population, energy demand is rising day by day. This not only depletes current energy reserves but also increases energy losses. Due to the limited potential of oil reserves, it is necessary to increase the use of alternative fuels. The use of hydrogen in combination with petroleum-derived fuels in internal combustion engines can reduce harmful exhaust emissions from fossil fuels. That is why researchers continue to work on an economical and safe fuel that does not harm the environment [1 - 5]. In addition to hydrogen-enriched petroleum fuels in internal combustion engines, various companies continue to work on fuel cells. One of the most important properties of hydrogen is that it does not harm the environment at the end of its combustion. With the development of

technology, the importance of hydrogen will increase for reasons such as increased production, cost reduction, and portability. Hydrogen is one of the important players in the clean energy sector. Hydrogen is a portable, storable, usable, and sustainable energy carrier in many different areas.

Over the past 30 years, extensive research has been conducted on the use of hydrogen as a fuel [6 - 8]. It is a directly usable energy source in the automotive sector with fuel cells. One of the most significant advantages of using hydrogen as a fuel in engines is that it reduces air pollution. Since there is no carbon in hydrogen fuel, there will be no emissions such as CO, CO₂, and HC at the end of combustion. When hydrogen energy is used in the transportation sector, which contributes to greenhouse effect, CO₂ emissions will be reduced. In a study conducted in Europe, it is estimated that by 2040,

new hydrogen vehicles will reduce CO₂ emissions by 35%, while hydrogen-powered public transport vehicles will reduce CO₂ emissions by 40%, with an average reduction in CO₂ emissions of 44.8 g/km [9].

Internal combustion engines are the most significant factors leading to an increase in environmental pollution [10 - 15]. The role of the internal combustion engine is to convert chemical energy into mechanical energy. In this engine, the system is renewed at each cycle. The system is in contact with only one heat source (the atmosphere and the fuel). Heat is produced by combustion in a variable volume chamber. It serves to increase the pressure within a gas filling this chamber (this gas is also initially composed of fuel and oxidizer: air). This increase in pressure results in a force exerted on a piston, a force that transforms the translational motion of the piston into the rotational motion of the shaft (crankshaft). The operation takes place in 4 stages: intake; compression; ignition (combustion); exhaust [11].

The most popular internal combustion engines are classified into two categories according to the ignition technique of the air-fuel mixture: spark ignition engines (gasoline engines) and compression ignition engines (Diesel engines).

A Diesel engine operates on the principle of self-ignition of the fuel. The richness of the mixture characterizes the engine load. The higher the load, the greater the quantity of injected fuel, while the airflow remains constant. When the piston rises in the combustion chamber (compression phase), it greatly increases the temperature and pressure, allowing the air-fuel mixture to self-ignite (the self-ignition potential of a fuel is characterized by the cetane number).

In a gasoline engine, the load is characterized by the airflow that varies depending on the load control. For an optimal compromise between performance, consumption, and emissions, gasoline engines operate around stoichiometry. Moreover, this promotes efficient operation of the three-way catalytic converter (for the three main pollutants: CO, NO_x, and HC). Indeed, the efficiency of this type of catalyst significantly degrades when deviating from stoichiometry.

Research indicates that most of the CO, HC, and NO_x compounds produced as a result of the combustion of fossil fuels come from gasoline and diesel engines. Harmful waste such as sulfur dioxide, lead, and soot are also present in the exhaust emissions of internal combustion engines [11], [16].

The sustainable use and production of hydrogen, which does not harm the environment, will be one possible solution. A hydrogen internal combustion engine vehicle is a type of hydrogen vehicle using an internal combustion engine. Hydrogen internal combustion engine vehicles are different from hydrogen fuel cell vehicles (which use hydrogen through electrochemical means rather than combustion). Instead, the hydrogen internal combustion engine is simply a modified version of the traditional gasoline internal combustion engine. Zero carbon means that no CO₂ is produced, thus eliminating the primary greenhouse gas emission from a conventional petroleum engine.

The characterization of an engine significantly affects its performance, leading to numerous studies aimed at optimizing engine performance. For instance, in [17], the surface of the combustion chamber is analyzed to understand heat transfer correlations. Similarly, the piston crown in relation to various combustion mode strategies

is investigated in [18]. The influence of fuel system variations on performance and emission characteristics is explored in [19], while [20] examines how combustion chamber geometry and fuel supply system variations can economize fuel consumption and reduce exhaust emissions. The impact of blended fuels with split injections on combustion and emission characteristics is analyzed in [21]. Additionally, [22] studies the effect of piston crown shape and the positioning of spark plugs and fuel injectors on fuel system control and emissions. Research in [23] delves into the use of hydrogen as a fuel for internal combustion engines, presenting a detailed analysis. Experimental studies focused on internal combustion engines fueled with hydrogen are also conducted in [24 - 25], offering valuable insights into the practical application and benefits of hydrogen as an alternative fuel. These comprehensive investigations collectively contribute to the advancement of engine design and fuel system optimization, highlighting the potential for improved efficiency and reduced environmental impact.

Motivated by the aforementioned studies, this research delves into the utilization of hydrogen as a fuel in an ICE, exploring a promising avenue towards reducing emissions and advancing sustainability in automotive propulsion systems. By leveraging the dynamic model initially developed for gasoline-powered ICEs, this study aims to adapt and extend it to accommodate the unique characteristics and operational parameters associated with hydrogen combustion. The goal is to construct a comprehensive and accurate dynamic model of an H₂-ICE, capable of simulating its performance under various operating conditions.

The proposed model facilitates further investigation into the effects of different components, including engine characterization, fuel characterization, and various methods of mixing fuel. For instance, by examining how hydrogen fuel impacts the combustion process, insights can be gained into optimizing fuel injection timing, air-fuel ratio, and ignition parameters to achieve efficient combustion and minimal emissions. Additionally, the model allows for the analysis of different hydrogen blending techniques and their effects on engine performance and emissions.

This study's dynamic model also provides a platform to explore the thermal management challenges unique to hydrogen combustion, such as its higher combustion temperature and faster flame speed compared to gasoline. Understanding these dynamics is crucial for designing effective cooling systems and ensuring engine durability. Moreover, the model can simulate the impact of hydrogen's lower energy density on fuel storage and delivery systems, offering insights into optimizing fuel tank design and refueling infrastructure for hydrogen-powered vehicles.

The effectiveness and fidelity of our proposed model will be rigorously assessed and validated using Matlab Simulink, a versatile platform widely employed for dynamic system modeling and simulation. Through meticulous calibration and validation against empirical data, we seek to ensure that our model accurately captures the dynamic behavior and performance nuances specific to hydrogen-fueled ICEs. This validation process is essential for establishing the reliability and predictive capability of our model, thus instilling confidence in its utility for subsequent analyses and optimization efforts.

2. Dynamic model of an H₂-ICE

Four-stroke internal combustion engines are the preferred choice

for conventional and hybrid vehicles due to their inherent fuel efficiency advantages over their two-stroke counterparts. This efficiency arises from the distinctive four-stroke engine cycle, where a power stroke occurs once every two revolutions of the crankshaft. This stands in contrast to two-stroke engines, which feature more frequent power strokes happening every revolution, resulting in higher fuel consumption per unit of power produced. Consequently, four-stroke engines boast reduced fuel consumption, emissions, and torque output compared to their two-stroke counterparts.

Key components of the four-stroke engine include the intake and exhaust manifold, intake and exhaust valves, spark plug, piston, coolant, cylinder, crankcase, connecting rod, and crankshaft. Each of these components plays a pivotal role in facilitating the engine's operation and performance. This study centers on the development of a comprehensive model for the four-stroke internal combustion engine, leveraging foundational research outlined in prior studies. Figure 1 provides a graphical representation of the fundamental operating principle of an internal combustion engine. It illustrates the sequential processes of intake, compression, power generation within the combustion chamber, and the subsequent transmission of torque to the crankshaft to drive the engine. Through meticulous modeling and analysis, this research aims to enhance our understanding of the intricate dynamics inherent to four-stroke engines, ultimately optimizing their performance in various automotive applications.

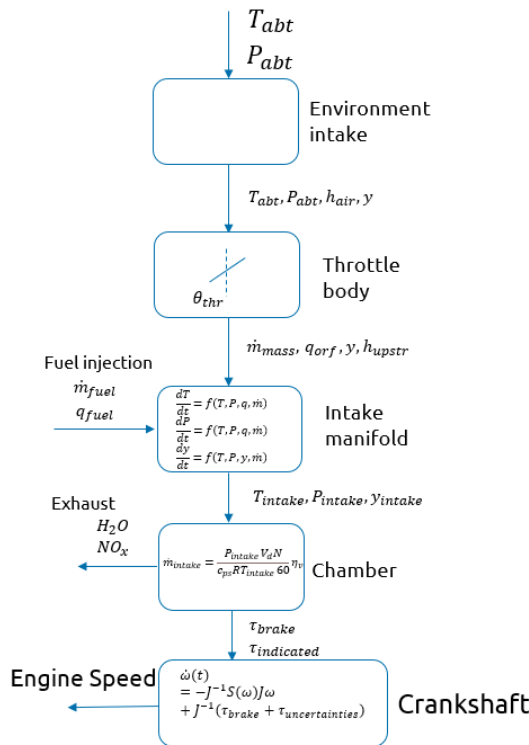


Figure 1. Representative operating diagram of the SI engine.

2.1. Intake Air System

The Intake Air System in an ICE is a crucial component responsible for delivering the appropriate amount of air to the engine's combustion chambers. Proper air intake is essential for efficient combustion and optimal engine performance. This system represents

the flow limit, which typically includes ambient temperature, pressure, specific enthalpy, and mass fraction (in the form of dry air). The ambient temperature and pressure (ambient temperature) can be constant or provided externally. The specific enthalpy is calculated as follows:

$$h_{air} = c_{p_{air}} T_{abt} \quad (1)$$

Where $c_{p_{air}}$ is the heat coefficient at constant and T_{abt} is the ambient temperature equal to 300K.

The mass fraction of dry air represents the percentage of different components in the inlet air, which are: Oxygen (O_2), Nitrogen (N_2), Unburned fuel (this component only appears after combustion), Carbon dioxide (CO_2), Water vapor (H_2O), Carbon monoxide (CO), Nitric oxide (NO), Nitrogen dioxide (NO_2), Nitric oxide and nitrogen dioxide (NO_x), Particulate matter, Air, Exhaust gases. Each component's mass fraction contributes to the overall composition of the inlet air, playing a crucial role in determining the system's behavior and performance characteristics.

2.2. Throttle Body

The throttle body is the part of the air intake system that controls the amount of air flowing into the engine, in response to driver accelerator pedal input in the main. The throttle body is usually located between the air filter box and the intake manifold, and it is usually attached to, or near, the mass airflow sensor. The mass flow rate through the throttle is determined as follow [16][26]:

The gas mass flow through the orifice:

$$\dot{m}_{orff} = \frac{A_{eff} P_{upstr}}{\sqrt{RT_{upstr}}} \Psi(P_{ratio}) \quad (2)$$

Where P_{ratio} is the ratio of downstream pressure (P_{dowstr}) and upstream pressure (P_{upstr}).

$$\Psi(P_{ratio}) = \begin{cases} \sqrt{\gamma \left(\frac{2}{\gamma+1}\right)^{\frac{\gamma+1}{\gamma-1}}} & \text{if: } P_{ratio} < \left(\frac{2}{\gamma+1}\right)^{\frac{\gamma}{\gamma-1}} \\ \sqrt{\frac{2\gamma}{\gamma-1} \left(\frac{P_{ratio}^{\frac{2}{\gamma}}}{-P_{ratio}^{\frac{\gamma+1}{\gamma}}}\right)} & \text{if: } \left(\frac{2}{\gamma+1}\right)^{\frac{\gamma}{\gamma-1}} < P_{ratio} < P_{lim} \\ \frac{P_{ratio}-1}{P_{lim}-1} \sqrt{\frac{2\gamma}{\gamma-1} \left(\frac{P_{lim}^{\frac{2}{\gamma}}}{-P_{lim}^{\frac{\gamma+1}{\gamma}}}\right)} & \text{if: } P_{lim} < P_{ratio} \end{cases} \quad (3)$$

Where $P_{upstr} = P_{abt} = 101325$ Pa is the ambient pressure. $\Psi(P_{ratio})$ is the based follow correlation and is the function of P_{ratio} calculates the based on the different conditions of flow.

$$P_{ratio} = \frac{P_{dowstr}}{P_{upstr}} \quad (4)$$

Where P_{lim} is the pressure ratio limitation, $\gamma = 1.4$ is the ratio of specific heats. The air mass flow rate (\dot{m}_{air}) then can be calculated as follows:

$$\dot{m}_{air} = \dot{m}_{orff} \gamma_{upstr_air} \quad (5)$$

Where γ_{upstr_air} is the upstream species mass fraction.

A_{eff} is the effect area, and is calculated as follows:

$$A_{eff} = \frac{\pi}{4} D_{thr}^2 C_{thr}(\theta_{thr}) \quad (6)$$

$$\theta_{thr} = \theta_{ct_thr} \frac{90}{100} \quad (7)$$

Where θ_{thr} is the open angle of the throttle (in degree), θ_{ct_thr} is the percentage of throttle body that open, D_{thr} is the throttle diameter at opening, $C_{thr}(\theta_{thr})$ is the discharge coefficient.

The heat flow rate q_{orf} of is calculated as follows:

$$q_{orf} = \dot{m}_{orf} h_{upstr} \quad (8)$$

Where h_{upstr} is the upstream specific enthalpy (h_{air}).

2.3. Intake Manifold

To calculate the fuel flow in the hydrogen (H_2) internal combustion engine, one utilizes the characteristics of the fuel injector along with the fuel injector pulse-width. The model for fuel flow is expressed as:

$$\dot{m}_{fuel} = \frac{N S_{inj} P_{w_{inj}} N_{cyl}}{c_{ps} 1000 * 60} \quad (9)$$

Where N represents engine speed in rpm, S_{inj} denotes the fuel injector slope, N_{cyl} signifies the number of engine cylinders, c_{ps} stands for the crankshaft revolutions per power stroke.

The fuel heat flow rate is subsequently determined by:

$$q_{fuel} = \dot{m}_{fuel} h_{upstr} \quad (10)$$

In contrast to gasoline spark-ignition (SI) engines, where gasoline is the sole fuel, in the case of hydrogen (H_2) engines, the fuel also serves as the intake gas. Therefore, the intake gas mass flow rate and its associated fuel heat flow must be corrected. The corrected intake gas mass flow rate (\dot{m}_{in_intk}) is calculated as the sum of the fuel mass flow rate (\dot{m}_{fuel}) and the gas mass flow rate (\dot{m}_{gas}).

$$\dot{m}_{in_intk} = \dot{m}_{fuel} + \dot{m}_{gas} \quad (11)$$

Similarly, the corrected intake gas heat flow (q_{in_intk}) is determined by summing the fuel heat flow (q_{fuel}) and the gas heat flow (q_{orf}).

$$q_{in_intk} = q_{fuel} + q_{orf} \quad (12)$$

Subsequently, the species mass fractions are reformulated as follows:

$$y_{unbrn_fuel} = \frac{\dot{m}_{fuel}}{\dot{m}_{in_intk}} \quad (13)$$

$$y_{air} = \frac{\dot{m}_{gas}}{\dot{m}_{in_intk}} \quad (14)$$

$$y_{O_2} = 0.233 \frac{\dot{m}_{gas}}{\dot{m}_{in_intk}} \quad (15)$$

$$y_{N_2} = 0.767 \frac{\dot{m}_{gas}}{\dot{m}_{in_intk}} \quad (16)$$

In this study, the other mass fractions remain zero. These formulations allow for a comprehensive understanding of the fuel and gas flows within the hydrogen internal combustion engine, facilitating

accurate modeling and analysis of its performance characteristics. The intake manifold serves as a critical component of the air intake system, responsible for regulating the pressure and temperature of the air delivered to the cylinder. The changes in temperature and pressure within the intake manifold are dynamically determined by employing a constant volume chamber model containing an ideal gas. This analysis leverages the continuity equation and the first law of thermodynamics to accurately characterize the behavior of the intake manifold. The rate changes in temperature and pressure are determined by implementing a constant volume chamber containing an ideal gas, the continuity equation and the first law of thermodynamics is used in this case as follows:

$$\frac{dT_{intake}}{dt} = \frac{RT_{intake}}{c_{p_air} V_{ch} P_{intake}} \left((q_{in_intk} \right. \quad (17)$$

$$\left. - T_{intake} c_v \dot{m}_{in_intk} \right)$$

$$\left. - (q_{out_intk} \right.$$

$$\left. - T_{intake} c_v \dot{m}_{out_intk} \right))$$

$$\frac{dP_{intake}}{dt} = \frac{P_{intake}}{T_{intake}} \frac{dT_{intake}}{dt} \quad (18)$$

$$+ \frac{RT_{intake}}{V_{ch}} (\dot{m}_{in_intk} - \dot{m}_{out_intk})$$

Where R is Ideal gas constant, V_{ch} is Chamber volume, T_{intake} and P_{intake} are the chamber absolute temperature and pressure respectively, q_{out_intk} is the output heat flow given by Eq. 17, and \dot{m}_{out_intk} is the mass flow in the chamber given by Eq. 25. Hence the specific enthalpy of the intake manifold is calculated as:

$$h_{intake} = c_{p_air} T_{intake} \quad (19)$$

Using the conservation of mass for each gas constituent, the mass fraction of gas in the chamber can be determined as follows:

$$\frac{dy_{intake}}{dt} = \frac{RT_{intake}}{V_{ch} P_{intake}} \left((y_{in_intk} \dot{m}_{in_intk} \right. \quad (20)$$

$$\left. - y_{intake} \dot{m}_{out_intk} \right)$$

$$+ y_{intake} (\dot{m}_{in_intk} - \dot{m}_{out_intk}))$$

These equations provide a comprehensive framework for understanding the dynamic behavior of temperature, pressure, and gas composition within the intake manifold, facilitating accurate modeling and analysis for optimizing engine performance.

To determine the output heat flow (q_{out_intk}), we employ a heat transfer model depicted in Figure 2. This model accounts for both convective and conductive heat transfer processes occurring within the intake manifold. The output heat flow is calculated as the sum of convective ($Q_{1,conv}$) and conductive ($Q_{1,cond}$) heat transfer components.

$$q_{out_intk} = Q_1 = Q_{1,conv} = Q_{1,cond} \quad (21)$$

$$Q_2 = Q_{2,conv} = Q_{2,cond} \quad (22)$$

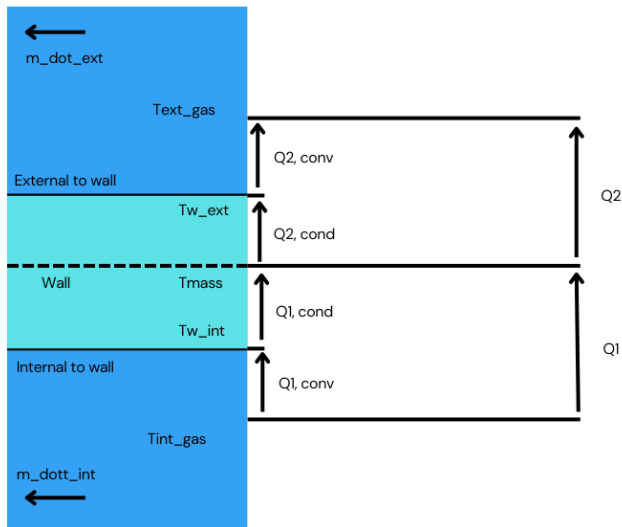


Figure 2. Heat transfer model

Firstly, $Q_{1,conv}$ represents the convective heat transfer from the intake gas to the interior wall of the manifold. It is computed using the equation:

$$Q_{1,conv} = c_{q,int}(\dot{m}_{in_intk})A_{int_conv}(T_{in_gas} - T_{w_int}) \quad (23)$$

Here, $c_{q,int}$ represents the convective heat transfer coefficient, \dot{m}_{in_intk} denotes the mass flow rate of the intake gas, A_{int_conv} is the convective surface area, T_{in_gas} is the temperature of the intake gas, and T_{w_int} represents the temperature of the interior wall of the intake manifold.

Secondly, $Q_{1,cond}$ denotes the conductive heat transfer from the interior wall of the manifold to the mass of the wall itself. It is given by:

$$Q_{1,cond} = \frac{k_{int}A_{int_cond}}{D_{int_cond}}(T_{w_int} - T_{mass}) \quad (24)$$

Where k_{int} is the thermal conductivity of the wall material, A_{int_cond} represents the conductive surface area, D_{int_cond} is the thickness of the wall, and T_{mass} denotes the temperature of the wall material.

Similarly, the heat transfer from the exterior wall of the manifold to the external environment is represented by $Q_{2,conv}$ and $Q_{2,cond}$. These components account for convective and conductive heat transfer processes, respectively, and are calculated using analogous equations, and are given as follows:

$$Q_{2,conv} = c_{q,ext}(ExtnlFlwVel)A_{ext_conv}(T_{w_ext} - T_{ext_gas}) \quad (25)$$

$$Q_{2,cond} = \frac{k_{ext}A_{ext_cond}}{D_{ext_cond}}(T_{mass} - T_{w_ext}) \quad (26)$$

Finally, the rate of change in temperature of the wall material

$(\frac{dT_{mass}}{dt})$ is determined by the difference between the input and output heat flows divided by the thermal capacity of the wall material as follows:

$$\frac{dT_{mass}}{dt} = \frac{Q_1 - Q_2}{c_{pwall}m_{wall}} \quad (27)$$

By incorporating Eq. (13) to Eq. (19) into this heat transfer model, we can accurately derive the output heat flow (q_{out_intk}), providing insights into the thermal dynamics of the intake manifold and facilitating optimization of heat management strategies for enhanced engine performance.

The Engine Cooling System serves several critical functions within the internal combustion engine (ICE) setup. Primarily, it acts to dissipate excess heat generated during engine operation, thereby preventing overheating and potential damage to engine components. Additionally, the cooling system plays a pivotal role in maintaining the engine at its optimal operating temperature, ensuring peak efficiency and performance. Furthermore, during engine startup, the cooling system facilitates the rapid attainment of the desired operating temperature, promoting smoother and more efficient engine operation from the outset.

In this study, our focus is not on designing the Engine Cooling System per se, but rather on integrating it seamlessly into our ICE system to form a closed-loop system. This integration is crucial for ensuring the overall functionality and efficiency of the ICE setup.

The temperature of the engine after undergoing the cooling process is governed by the following equation:

$$\frac{dT_{cooling}}{dt} = \frac{\dot{m}_{out_intk}(c_{p_air}T_{intake} - c_{p_air}T_{exh}) + LHV\dot{m}_{fuel} - \tau\omega}{c_{eng}} \quad (28)$$

Where LHV is the fuel lower heating value, ω is the engine speed in rad/s. $c_{eng} = 40000$ is the heat capacity.

The H₂-ICE model employed in this study is based on the Spark-Ignition (SI) engine model, with hydrogen (H₂) serving as a substitute for gasoline. This choice reflects a shift towards cleaner and more sustainable fuel alternatives, aligning with the broader objective of reducing emissions and promoting environmental sustainability in automotive applications.

By incorporating the Engine Cooling System into our H₂-ICE model, we can ensure the holistic simulation and analysis of the entire engine system, enabling comprehensive assessments of performance, efficiency, and thermal management strategies. This integrated approach lays the foundation for advancing the development and optimization of hydrogen-powered internal combustion engines for future automotive applications.

2.4. Air Mass Flow Model

To calculate the air mass flow in the engine chamber, one shall use a speed-density air mass flow model as depicted in Figure 3. The speed-density model uses the speed-density equation to calculate the engine air mass flow. The equation relates the engine air mass flow to the intake manifold gas pressure, intake manifold gas temperature, and engine speed. Consider using this air mass flow model in simple

conventional engine designs, where variable valvetrain technologies are not in use.

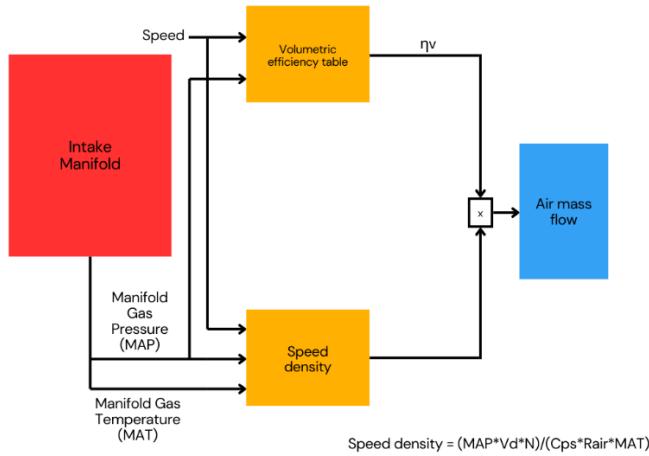


Figure 3. Engine Chamber Speed-Density Air Mass Flow Model

To determine the air mass flow, the speed-density air mass flow model applies these speed-density equations at the intake manifold gas pressure and gas temperature states.

The mass flow (\dot{m}_{intake}) at the intake port can be calculated as follows [16]-[26]:

$$\dot{m}_{intake} = \frac{P_{intake} V_d N}{c_{ps} R T_{intake} 60} \eta_v \quad (29)$$

Where η_v is engine volumetric efficiency as given in Figure 4, dimensionless, is a function of intake manifold absolute pressure (P_{intake}) and engine speed (N) and calculated as follows:

$$\eta_v = f(P_{intake}, N) = \dot{m}_{intake} \frac{c_{ps} R T_{intake} 60}{P_{intake} V_d N} \quad (30)$$

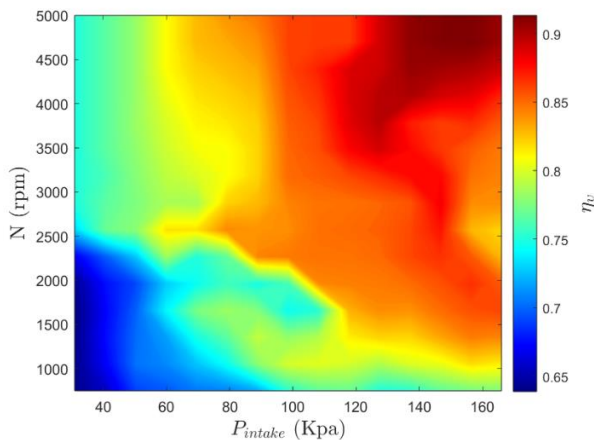


Figure 4. Engine volumetric efficiency

Subsequently, the calculated air mass flow is multiplied by the mass fraction of air (y_{intake_air}) in the intake mixture to determine the air mass (\dot{m}_{air_intake}):

$$\dot{m}_{air_intake} = y_{intake_air} \dot{m}_{intake} \quad (31)$$

Furthermore, the engine load (L_{eng}), a crucial parameter indicative of the engine's operational state, is derived using the formula:

$$L_{eng} = \frac{\dot{m}_{air_intake} c_{ps} * 60 R T_{std}}{V_d N P_{std}} \quad (32)$$

Where T_{std}, P_{std} are the standard temperature and pressure respectively.

The Air-Fuel ratio is calculated as:

$$ARF = \frac{\dot{m}_{air_intake}}{\dot{m}_{fuel}} \quad (33)$$

2.5. Torque Model

In the SI engine the indicated torque means that the torque or power of the engine is evaluated in the scope of thermodynamics (pressure and volume of cylinder), not including any mechanical losses in the whole power development and transmission process conceptually illustrates pressure variation in a cylinder along with crankshaft rotation angle. This torque is calculated as follows [11]:

$$\tau_{indicated} = \frac{P_{indicated} * 60}{2\pi N} \quad (34)$$

Where $P_{indicated}$ is the indicated power and can be calculated as:

$$P_{indicated} = \dot{m}_{fuel} * LHV \eta_{indicated} \quad (35)$$

Where $\eta_{indicated}$ is the engine indicated load efficiency as well as a function of engine speed (N) and indicated torque ($\tau_{indicated}$) as depicted in Figure 5.

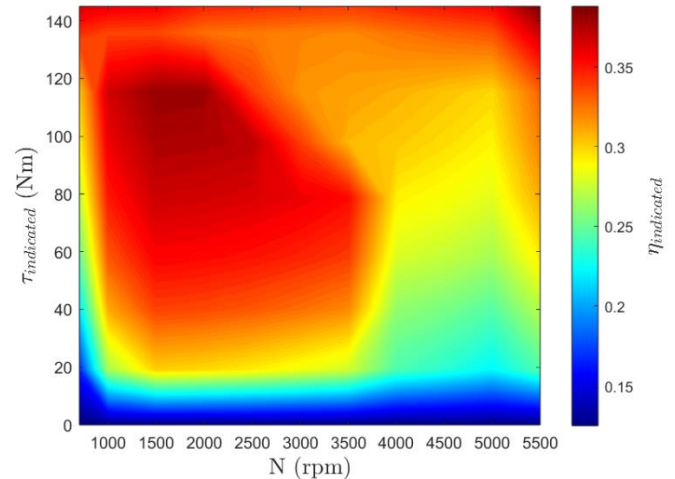


Figure 5. Indicated torque efficiency

Not all the torque produced in the cylinder (indicated power and torque) are available on the crankshaft. The available torque on the crankshaft is the difference between the indicated torque and friction torque, respectively, expressed as:

$$\tau_{brake} = \tau_{indicated} - \tau_{friction} \quad (36)$$

The basic engine accessories include a water pump, oil pump, fuel pump, and valve shaft. Other accessories may depend on applications, such as cooling fan, alternator, power steering pump, and air conditioner compressor. In an engine test, the accessories that are driven by the engine crankshaft should be clearly specified. All

power and torque requirements for driving accessories and overcoming frictions are grouped together and called the friction torque and is given as:

$$\tau_{friction} = \eta_{friction} f(L_{eng}, N) \tag{37}$$

where $\eta_{friction}$ is the friction temperature factor as demonstrated in Figure 7, $f(L_{eng}, N)$ is the function of engine load (L_{eng}) and engine speed (N) as depicted in Figure 6.

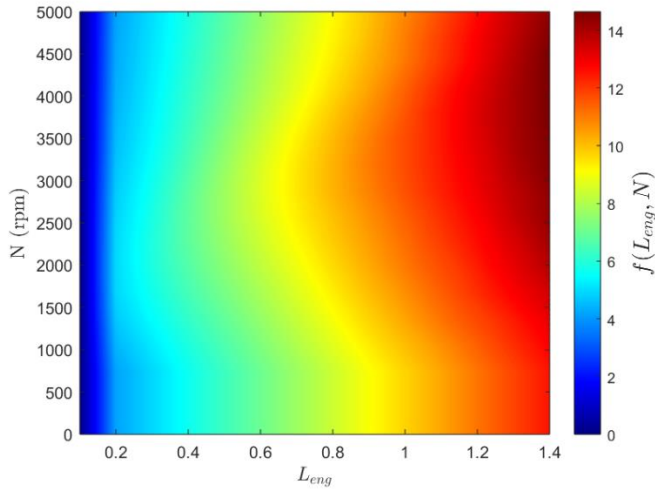


Figure 6. Friction force factor

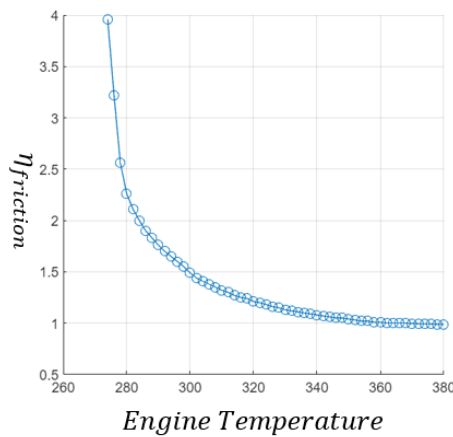


Figure 7. Friction temperature factor

3. Simulation Results and Discussion

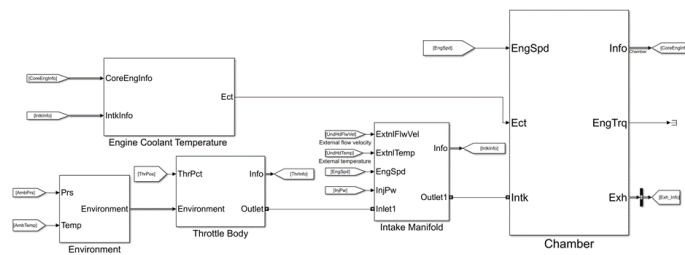


Figure 8. Detailed Simulink model for ICE

To illustrate the performance of the developed model, an explicative simulation will be conducted using Matlab Simulink, as shown in Figure 8. The simulation will utilize input references for the throttle valve open angle, given in Figure 9, and the fuel injector pulse-width, given in Figure 10, to demonstrate the model's performance. The scenario involves first regulating the throttle valve's open angle according to Figure 9, and then injecting hydrogen fuel into the engine following the values in Figure 10. This simulation aims to show how the throttle valve configuration affects overall system behavior, examining the relationship between throttle position and fuel injector pulse-width in controlling the air and fuel intake. Expected outcomes include insights into air intake dynamics, pressure, temperature, fuel injection response, combustion efficiency, and overall engine performance, such as power output, torque, and engine velocity. By integrating these findings, a comprehensive understanding of the throttle valve's influence on system behavior is achieved, providing a foundational step towards optimizing system design and enhancing operational efficiency. This detailed analysis ultimately validates the proposed H2-ICE model and offers valuable insights for further research and development in hydrogen-fueled automotive technologies.

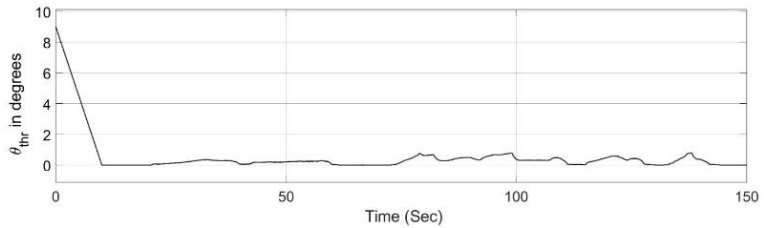


Figure 9. Throttle angle

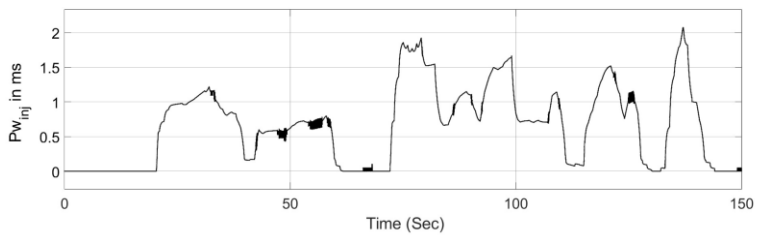


Figure 10. Fuel injector pulse-width

The ambient temperature and pressure are set up as 300 °K and 101325 Pa respectively, the Heat coefficient at constant $c_{p,air} = 1005 \text{ J/(kg}\cdot\text{K)}$. We consider the dry air contains only oxygen and nitrogen with its mass fraction are given as $y_{O_2} = 0.233$ and $y_{N_2} = 0.767$.

The downstream pressure within the intake manifold is calculated by applying Eq. (18), and the outcomes are meticulously presented in Figure 11. Subsequently, this calculated downstream pressure serves as a crucial parameter in determining the pressure ratio, as stipulated by Eq. (3), where the upstream pressure aligns with the ambient pressure. With this pressure ratio established, as graphically depicted in Figure 12, an essential step ensues in discerning the base flow correlation governing the gas mass flow through the orifice (2). This correlation is meticulously illustrated and analyzed in detail, offering valuable insights into the dynamics of gas flow within the system.

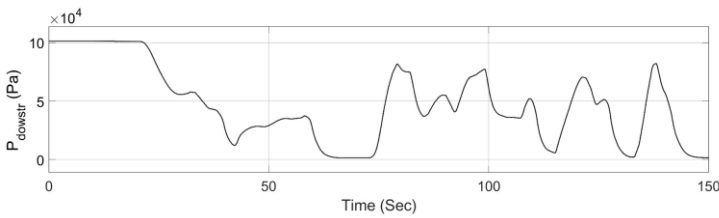


Figure 11. Downstream pressure in the intake manifold

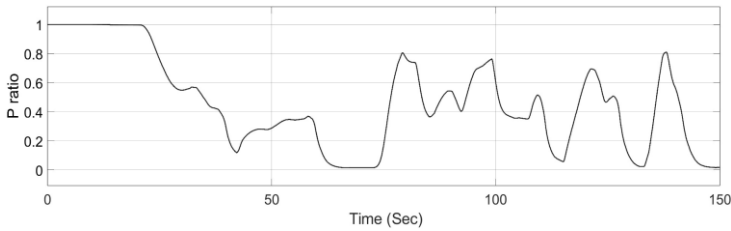


Figure 12. Pressure Ratio

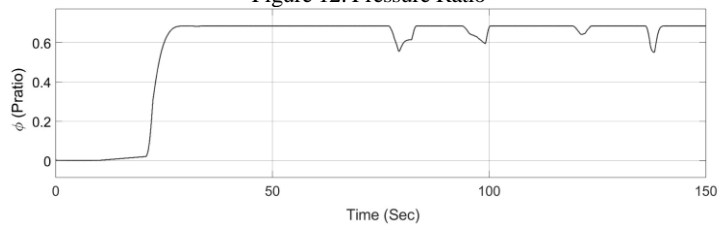


Figure 13. Base flow correlation

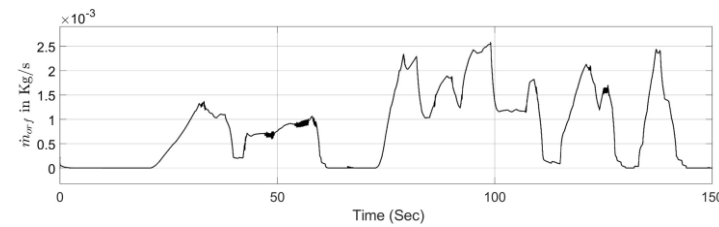


Figure 14. Gas mass flow through the orifice

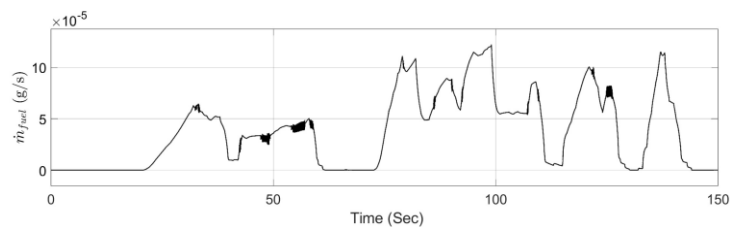


Figure 15. Fuel mass flow rate

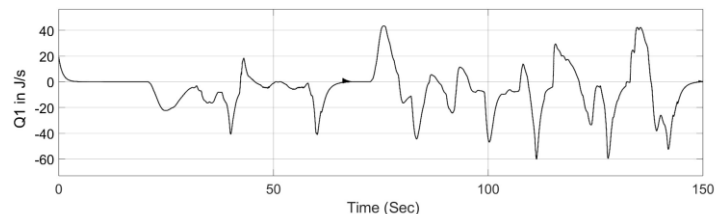


Figure 16. Output heat flow rate

Figures 13 present a comprehensive visualization of this base flow correlation, enriching our understanding of the intricate interplay between pressure differentials and gas mass flow rates as presented in Figure 14. This detailed analysis not only elucidates the fundamental principles governing gas flow behavior but also provides practical

insights crucial for optimizing system performance and efficiency. Within this simulation, hydrogen fuel injection into the intake manifold is implemented, with the corresponding fuel mass flow rate depicted in Figure 15. These parameters play a pivotal role in regulating the combustion process within the engine, ensuring optimal fuel-air mixture ratios and combustion efficiency. By accurately modeling and analyzing the fuel injection dynamics, insights into engine performance, fuel consumption, and emissions can be gleaned. This comprehensive examination of fuel injection characteristics enriches our understanding of engine behavior under varying operating conditions and facilitates the refinement of engine control strategies for enhanced performance and efficiency.

Utilizing the thermal dynamic equations of Eq. (21) to Eq. (27), the heat flow from the internal gas to a specified wall depth, termed as the output heat flow, can be accurately determined. This crucial parameter, which characterizes the heat transfer process within the system, is meticulously presented in Figure 16. Additionally, the heat transfer rate, representing the rate at which heat is exchanged between the gas and the surrounding walls, is quantified based on the same equations and visually depicted in Figure 17.

These analyses offer valuable insights into the thermal dynamics of the system, shedding light on heat distribution, dissipation, and overall thermal performance. By comprehensively understanding the heat transfer processes, engineers can optimize system design, enhance thermal efficiency, and mitigate thermal-related issues, thereby ensuring reliable and efficient operation under diverse operating conditions.

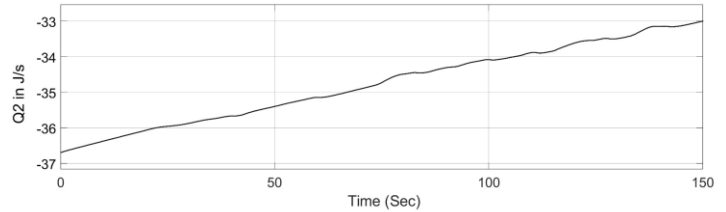


Figure 17. Heat transfer rate

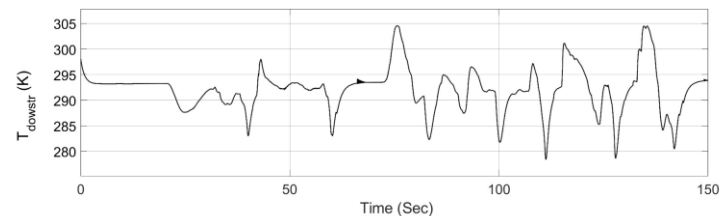


Figure 18. Downstream (intake) temperature

Given the determined output heat flow rate, it becomes feasible to ascertain the intake temperature, also referred to as the downstream temperature, as outlined in Eq. (17). This temperature parameter plays a pivotal role in regulating engine performance and combustion efficiency. By accurately modeling and analyzing the heat transfer dynamics within the system, insights into the variation of intake temperature under different operating conditions can be gained. Figure 18 visually presents these temperature variations, offering a comprehensive understanding of how heat transfer processes influence

intake temperature. This analysis enables engineers to optimize engine operation, ensuring that intake temperatures remain within desired ranges to promote efficient combustion and mitigate potential thermal-related issues.

The mass fraction in the downstream of the intake manifold is determined using Eq. (20), which accounts for various factors influencing the composition of gases within the system. By applying this equation, the simulation yields valuable insights into the downstream mass fraction, representing the proportion of different gas components present in the intake manifold. Figure 19 visually illustrates

the results of this simulation, offering a comprehensive depiction of how the mass fraction varies under different operating conditions. This analysis enhances our understanding of gas composition dynamics within the intake manifold, providing essential information for optimizing combustion processes, controlling emissions, and ensuring efficient engine operation. By closely examining the downstream mass fraction, engineers can make informed decisions regarding fuel-air mixture ratios and combustion strategies, ultimately optimizing engine performance and reducing environmental impact.

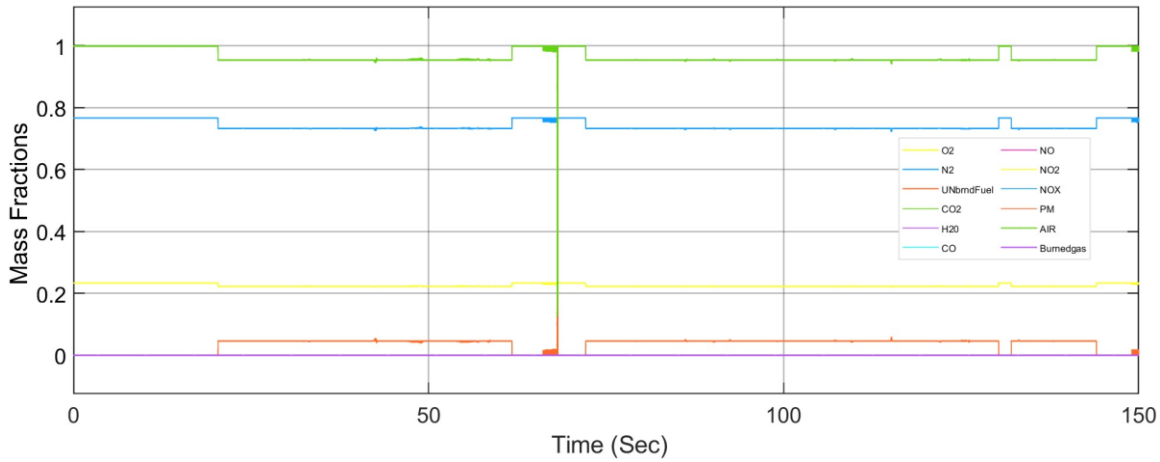


Figure 19. Downstream Mass Fraction

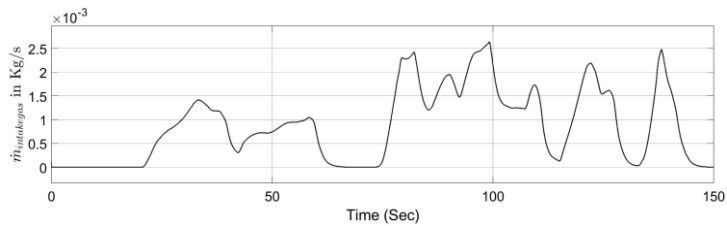


Figure 20. Gas mass flow rate in the chamber

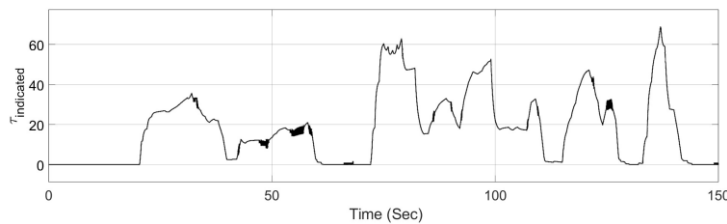


Figure 21. Engine indicated torque

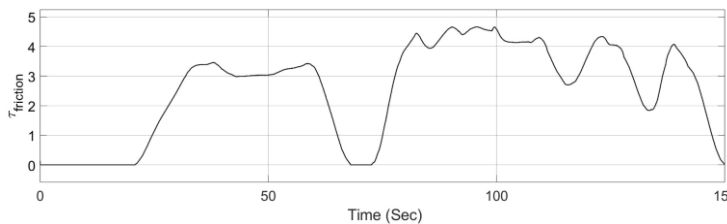


Figure 22. Friction torque

Figure 20 depicts the gas mass flow rate within the chamber, providing crucial insights into the dynamics of gas flow through the engine system. This parameter serves as a fundamental metric for evaluating engine performance and efficiency. Subsequently, utilizing the gas mass flow rate data, the indicated torque can be determined according to Eq. (35), as illustrated in Figure 22. This torque represents the theoretical output torque generated by the engine, reflecting the mechanical power produced during the combustion process. Conversely, Figure 22 presents the friction torque, which accounts for mechanical losses within the engine system.

By comparing the indicated torque with the friction torque, engineers can assess the overall efficiency and mechanical integrity of the engine. Finally, Figure 23 shows the engine speed, providing valuable insights into the rotational speed of the engine's crankshaft under varying operating conditions. Together, these parameters offer a comprehensive understanding of engine performance, enabling engineers to optimize design parameters, refine control strategies, and enhance overall operational efficiency.

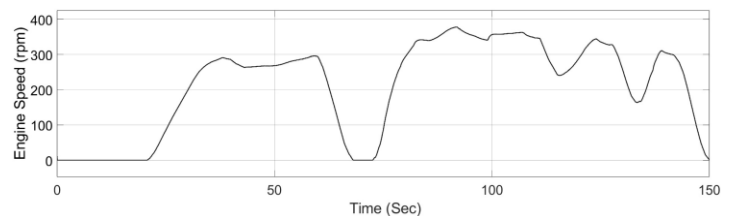


Figure 23. Engine speed

4. Conclusions

In conclusion, this study has centered on the examination of hydrogen's potential as an alternative fuel for proposed hydrogen-powered internal combustion engine (H₂-ICE). Through the adaptation of a dynamic model originally designed for gasoline, a comprehensive dynamic model tailored specifically for ICEs fueled by hydrogen has been successfully developed. This approach underscores the increasing significance of hydrogen as a sustainable energy carrier, presenting a promising pathway towards cleaner transportation solutions. Throughout the simulation results, the effectiveness of the H₂-ICE model was demonstrated using the throttle valve open angle and fuel injector pulse width as references. The model accurately reflected the dynamic behavior of the engine under varying conditions, showcasing its potential for optimizing performance and efficiency. The findings underscore the model's capability to simulate real-world scenarios, providing valuable insights for future research and development in hydrogen-fueled engines. This study highlights the viability of hydrogen as an alternative fuel, contributing to the advancement of sustainable and environmentally friendly automotive technologies. The exploration into the intricate dynamics of hydrogen-powered internal combustion engines contributes substantially to ongoing research and development efforts aimed at advancing cleaner and potentially more efficient automotive technologies. By delving into the operational intricacies of these engines, this study lays the groundwork for future optimization and design endeavors within the realm of hydrogen-powered vehicles. Furthermore, this work not only addresses the pressing need for sustainable energy solutions but also opens up new avenues for innovation and advancement in the field of hydrogen vehicles. Through the successful adaptation and validation of the dynamic model for H₂-ICE, valuable insights into their operational characteristics, efficiency are provided, thus facilitating informed decision-making and strategic planning in the automotive industry.

Acknowledgment

This work was carried out at Altran Prototypes Automobiles (APA) as a part of the Intelligence & Innovation Powertrain project within the Capgemini Engineering Research and Innovation Department.

Nomenclature

T_{abt}	300	Ambient temperature (K)
P_{abt}	101325	Ambient pressure (Pa)
h_{air}		Ambient enthalpy (J/kg)
$c_{p,air}$	1005	Heat coefficient at constant pressure (J/(kgK))
q_{orf}		Heat flow rate (J/s)
h_{upstr}		Upstream specific enthalpy (J/kg)
R	287	Ideal gas constant (J/(kgK))
A_{eff}		Effective cross area
$C_{thr}(\theta_{thr})$		Discharge coefficient
$\theta_{ct,thr}$		Percentage of throttle body that open (%)
γ		Ratio of specific heats
P_{ratio}		Pressure ratio
P_{lim}		Pressure ratio limit
P_{upstr}		Upstream pressure (Pa)
P_{dowstr}		Downstream pressure (Pa)

$y_{upstr,air}$	1	Upstream species air mass fraction
\dot{m}_{orf}		Gas mass flow through the orifice
\dot{m}_{air}		Air mass flow
θ_{thr}		Open angle of the throttle (deg)
D_{thr}		Throttle diameter at opening (m)
Q_1		Heat flow from the internal gas to a specified wall depth (J/s)
$Q_{1,conv}$		Heat flow convection from the internal gas to the internal wall (J/s)
$Q_{1,cond}$		Conduction heat transfer rate (J/s)
Q_2		Heat transfer rate (J/s)
$Q_{2,conv}$		Convection heat transfer (J/s)
$Q_{2,cond}$		Heat flow conduction from the external middle portion of the wall to the external wall (J/s)
T_{intake}		Chamber absolute temperature (K)
P_{intake}		Chamber absolute pressure (Pa)
h_{intake}		Specific enthalpy of the intake manifold (J/kg)
$\dot{m}_{in,intk}$		Chamber input mass flow (kg/s)
$\dot{m}_{out,intk}$		Chamber output mass flow (kg/s)
$q_{in,intk}$		Chamber input heat flow (J/s)
$q_{out,intk}$		Chamber output heat flow (J/s)
$y_{in,intk}$		Input species mass fraction
y_{intake}		Species mass fraction in the chamber
$T_{in,gas}$		Temperature of the gas inside the chamber (K)
$T_{w,int}$		Temperature of the inside wall of the chamber (K)
$T_{ext,gas}$		External gas temperature (K)
$T_{w,ext}$		Temperature of the external wall of the chamber (K)
T_{mass}		Temperature of the thermal mass (K)
k_{int}	25	Thermal conductivity (W/(mK))
$A_{int,cond}$	0.003	Internal conduction area (m ²)
$A_{int,conv}$	0.125	Internal convection area (m ²)
$D_{int,cond}$	0.004	Internal wall thickness (m)
k_{ext}	25	External wall thermal conductivity (W/(mK))
$A_{ext,cond}$	0.003	External conduction area (m ²)
$A_{ext,conv}$	0.125	External convection area (m ²)
$D_{ext,cond}$	0.004	External wall thickness (m)
$c_{q,int}$		Internal convection heat transfer coefficient (W/(m ² K))
$c_{q,ext}$		External convection heat transfer coefficient (W/(m ² K))
$c_{p,wall}$	900	Wall heat capacity (J/(kgK))
m_{wall}	7	Thermal mass (kg)
V_{ch}	29e-4	Chamber volume (m ³)
$ExtnlFlwVel$		External flow velocity
\dot{m}_{fuel}		Fuel mass flow (g/s)
N		Engine speed (rpm)
S_{inj}	6.4516	Fuel injector slope (mg/ms)
$P_{w,nj}$		Fuel injector pulse-width (ms)
N_{cyl}	4	Number of engine cylinders
c_{ps}	2	Crankshaft revolutions per power stroke
$T_{cooling}$		Engine cooling temperature (K)
c_{eng}	40000	Heat capacity
LHV	473e5	Fuel lower heating value (J/kg)
\dot{m}_{fuel}		Fuel mass flow (kg/s)
T_{exh}		Exhaust temperature (K)
τ		Engine brake torque (Nm)
ω		Engine speed (rad/s)

\dot{m}_{intake}		Intake gas mass flow in the chamber (kg/s)
V_d		Displaced volume
L_{eng}		Engine load
η_v		Engine volumetric efficiency
$\eta_{indicated}$		Indicated load efficiency
$\eta_{friction}$		Friction temperature factor
$\tau_{indicated}$		Indicated torque (Nm)
τ_{brake}		Brake torque (Nm)
$\tau_{friction}$		Friction torque (Nm)
ARF		Air fuel ratio
T_{std}	293.15	Standard temperature (K)
P_{std}	101325	Standard pressure (Pa)

Conflict of Interest Statement

Q-T.D and F.H contributed equally. All authors have given approval to the final version of the manuscript. The authors declare that there is no conflict of interest in the study. The authors would also like to thank Guillaume Guilbert who have contributed immensely for the part of the project.

CRediT Author Statement

Fatima Haidar: Writing- review & editing, supervision, project administration & validation. **Quang Truc Dam:** Writing original draft & formal analysis, review & validation. **Nour Mama:** formal analysis & Simulation. **Sherwin Joy Chennapalli:** formal analysis & Simulation

References

- Akal, D., Öztuna, S., & Büyükakın, M. K. (2020). A review of hydrogen usage in internal combustion engines (gasoline-Lpg-diesel) from combustion performance aspect. *International Journal of Hydrogen Energy*, 45(60), 35257–35268.
- Arslan, T. A. (2023). A Comprehensive Review on Stirling Engines. *Engineering Perspective*, 3(3), 42–56.
- Gandhi, R. (2015). Use of Hydrogen in Internal Combustion Engine. *International Journal of Engineering and Technical Research*.
- Knorr, H., Held, W., Prüm, W., & Rüdiger, H. (1998). The man hydrogen propulsion system for city buses. *International Journal of Hydrogen Energy*, 23(3), 201–208.
- Milojević, S. (2016). Reconstruction of Existing City Buses on Diesel Fuel For Drive on Hydrogen. *Applied Engineering Letters*, 16–23.
- Karagöz, Y. (2017). EFFECT OF HYDROGEN ADDITION AT DIFFERENT LEVELS ON EMISSIONS AND PERFORMANCE OF A DIESEL ENGINE. *Journal of Thermal Engineering*, 1780–1790.
- Stępień, Z. (2021). A Comprehensive Overview of Hydrogen-Fueled Internal Combustion Engines: Achievements and Future Challenges. *Energies*, 14(20), 6504.
- Karakaş, O., Şeker, U. B., & Solmaz, H. (2021). Modeling of an Electric Bus Using MATLAB/Simulink and Determining Cost Saving for a Realistic City Bus Line Driving Cycle. *Engineering Perspective*, 2(2), 52–62.
- Li, X., Zhuang, Y., Wang, Y., Zhu, Z., Qian, Y., & Zhai, R. (2024). An experimental investigation on the lean-burn characteristics of a novel hydrogen fueled spark ignition engine: Hydrogen injection via a micro-hole on the spark plug. *International Journal of Hydrogen Energy*, 57, 990–999.
- Shadidi, B., Najafi, G., & Yusaf, T. (2021). A Review of Hydrogen as a Fuel in Internal Combustion Engines. *Energies*, 14(19), 6209.
- Ehsani, M., Yimin, G., Stefano, L., & Kambiz Ebrahimi, M. (2018). *Modern Electric, Hybrid Electric, and Fuel Cell Vehicles*, Third Edition. CRC Press.
- Singh, A. P., Sharma, N., Agarwal, R., & Agarwal, A. K. (Eds.). (2020). *Advanced Combustion Techniques and Engine Technologies for the Automotive Sector*. Springer Singapore.
- Bayrakçeken, H. (2023). Effect of Clutch Pedal Distances on Fuel Consumption Under Actual Operating Conditions. *Engineering Perspective*, 4(4), 63–67.
- Biswas, S., & Ekoto, I. (2020). Ozone Added Spark Assisted Compression Ignition. In A. P. Singh, N. Sharma, R. Agarwal, & A. K. Agarwal (Eds.), *Advanced Combustion Techniques and Engine Technologies for the Automotive Sector* (pp. 159–185). Springer Singapore.
- Nagareddy, S. (2017). Temperature Distribution Measurement on Combustion Chamber Surface of Diesel Engine -Experimental Method.
- Heywood, J. B. (2018). *Internal combustion engine fundamentals* (Second revised edition). McGraw-Hill Education.
- Kumar, S., Kumar, A., Sharama, A. R., & Kumar, A. (2018). Heat Transfer Correlations on Combustion Chamber Surface of Diesel Engine—Experimental Work. *International Journal of Automotive Science and Technology*, 2(3), 28–35.
- Kumar, S. (2020). Piston Crown Profile Modifications for Various Combustion Mode Strategies of Modified GDI Engine towards NOx and PM Reduction. *International Journal of Automotive Science and Technology*, 4(4), 289–294.
- Nagareddy, S., & Govindasamy, K. (2022b). Influence of fuel system variations on performance and emission characteristics of combined air-wall-guided mode modified GDI engine with alcoholic fuels and exhaust gas recirculation. *Environmental Science and Pollution Research*, 30(22), 61234–61245.
- Nagareddy, S., & Govindasamy, K. (2022a). Combustion chamber geometry and fuel supply system variations on fuel economy and exhaust emissions of GDI engine with EGR. *Thermal Science*, 26(2 Part A), 1207–1217.
- Shivakumar N., Vijayakumar K., Surendran, A., Jose, C., & Mahmood V. K., S. (2023). Impact of blended fuels with split injections on combustion and emission characteristics of spray guided mode modified GDI engine. 020147.
- Nagareddy, S., & Govindasamy, K. (2022). Influence of piston crown shape with different positions of spark plug and fuel injector, %EGR, and fuel system control on emissions from modified GDI engines compared with a base diesel engine. *Transactions of the Canadian Society for Mechanical Engineering*, 46(2), 355–364.
- Falfari, S., Cazzoli, G., Mariani, V., & Bianchi, G. (2023). Hydrogen Application as a Fuel in Internal Combustion Engines. *Energies*, 16(6), 2545.
- Azeem, N., Beatrice, C., Vassallo, A., Pesce, F., Gessaroli, D., Biet, C., & Guido, C. (2024). Experimental study of cycle-by-cycle variations in a spark ignition internal combustion engine fueled with hydrogen. *International Journal of Hydrogen Energy*, 60, 1224–1238.
- Ricci, F., Zembi, J., Avana, M., Grimaldi, C. N., Battistoni, M., & Papi, S. (2024). Analysis of Hydrogen Combustion in a Spark Ignition Research Engine with a Barrier Discharge Igniter. *Energies*, 17(7), 1739.
- Stone, R. (1992). *Introduction to Internal Combustion Engines* (Second edition). The Macmillan Press LTD.



Effects of CNC Tool Runouts on Drilling Process

M. Kubilay Askerden^{1*} , Mustafa Yazar² , Şükrü Talaş³ 

¹ Mechanical Engineering Department, Uludag University, Bursa, Turkey

² Şahinkul Machinery and Spare Parts Industry. Trade A.S, Bursa, Turkey

³ Metallurgical and Materials Engineering Department, Afyon Kocatepe University, Afyon, Turkey

ABSTRACT

In this study, the surface roughness, dimensional accuracy and tool life that tool runout caused by CNC spindle mechanism based on metal mold manufacturing were investigated. In order to understand tool runout, spindle health measurement was performed: runout measurement with 300 mm test bar, spindle conical runout measurement, spindle pull force measurement and again spindle bearing vibration values were examined. In this study, spindle maintenance was performed and its effects on the final product before and after maintenance were investigated. Holes were drilled with 1, 2 and 3 times the drill diameter, the dimensional accuracy of the holes, the effect of runout on surface roughness in the hole drilling process and the runout and life of the drill bit used were investigated. The effects of runout before and after the maintenance were compared. Elimination of tool runout positively affected the surface roughness and parts with lower surface roughness were obtained. It positively affected the dimensional accuracy and the measurement tolerance was narrowed. Since the effect of tool runout on the cutting tool life is eliminated, its life is extended and the consumable cost is reduced. It has been observed that tool runout has a negative effect on machining in the hole drilling process with this experimental study.

Keywords: Tool Runout, Tool Life, Periodic Maintenance, Drilling

History

Received: 11.06.2024

Accepted: 03.09.2024

How to cite this paper:

Author Contacts

*Corresponding Author

e-mail addresses : mkaskerden@gmail.com, yazatmustafa08@gmail.com, stalas@aku.edu.tr

Askerden, M.K., Yazar, M., Talaş, Ş., (2024). Effects of CNC Tool Runouts on Drilling Process. Engineering Perspective, 4 (3), 119-124. <http://dx.doi.org/10.29228/eng.pers.77964>

1. Introduction

Drilling is a critical operation in addition to surface treatment during mould manufacturing, and it is an important machining step among many industrial metalworking methods. It has been reported to account for more than 40% of the processing rate in the processing of metals. [1]. The run-out that will occur in the tool in these operations is a phenomenon that significantly affects the tool life, geometric tolerances and machining costs and can cause significant financial losses if not taken into account. In drilling, the radial cutting force at the drill bit is critical to tool damage and ease of machining. Therefore, tool geometries are designed to reduce the cutting force. Run-out occurs when the rotating parts do not rotate axially in line. Run-out in drilling operations, that is, uneven cutting forces imposed on the tool edges, cause tool displacement, damage to the drill surface, and this leads to errors such as wear during boring and guide shafts working inside the hole [2, 3,4]. Tool run-out greatly affects the actual cutting radius of the tool; negatively affects the quality and efficiency of the processes. There are many simulations, models and studies on this

subject; these operations enable cutting operations that lead to better surface accuracy, higher productivity and longer tool life [5]. Positional deviation of the spindle from the rotation axis during the drilling process can often be observed even at the beginning of the operation. This deviation is caused by the axial deviation of the tool rotation axis at the cutting edge. Experimental results show that drill protrusion length has a significant effect on hole position accuracy [6]. Matsumura et al. developed a force model to analyze drilling operations with cutter run-outs. In this developed force model simulation, three-dimensional chip flow in the drilling process is modelled by stacking orthogonal cuts on the planes containing the cutting and chip flow directions. With the force model presented, it was found that when the cutter run-out increased in the drilling of Aluminium (Al) pressure casting, the thrust decreased significantly [2].

Tool runout is triggered by not performing periodic maintenance of the cone, spindle bearings and drawbar springs that the tool is attached to on the spindle. These structures are shown in Figure 1. Periodic maintenance brings together many benefits such as production efficiency and longer use of the machine. [7].

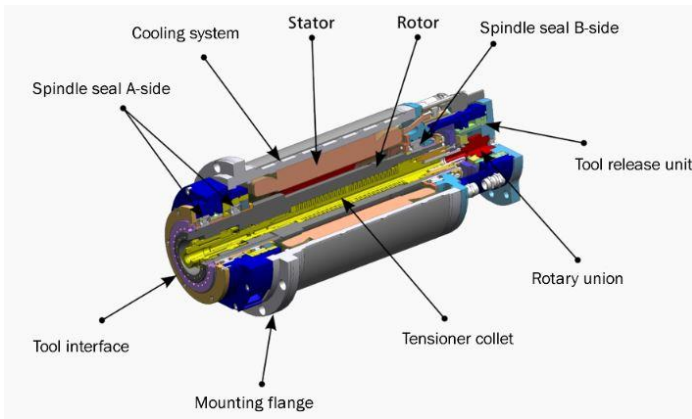


Figure 1. Appearance layout of CNC spindle parts [8]

The performance of a CNC machine tool depends on the accuracy of the machine to determine whether the end product conforms to the manufacturing specification. The accuracy of the machine must be measurable and analysable, so the effect of errors can be estimated on a workpiece. These errors can be eliminated by periodic maintenance and their effects on the final product can be minimized [9]. Considering the effect of spindle speed for cutter run-out, Zhang et al. proposed an effective non-contact calibration method and discussed the effect of cutter run-out on the mechanics and dynamics of the cutting process. The proposed models have been successfully validated by a series of experiments. Zhang et al., in their study, show that cutter run-out is dependent on spindle speed due to the variation of the vibration response of the spindle system under different spindle speeds [10]. An approach for modelling the milling process geometry with cutter run-out based on the actual tooth trajectory of the cutter in the milling process was proposed by Li et al. In these studies, it was observed that variable chip loads and variable wear on teeth were observed in evaluating the effects of cutter run-out using models [11].

The cutting tool run-out occurs in two different ways, radial and axial (Figure 2). Tool run-out is a phenomenon that affects geometry accuracy in the cutting process and is neglected in most of the studies on tool path planning. A new approach is presented for integrating the cutter run-out effect into envelope surface modelling and toolpath optimization for five-axis side milling with a tapered cutter. The results show that geometry errors caused by run-out can be significantly reduced by using the proposed method [13].

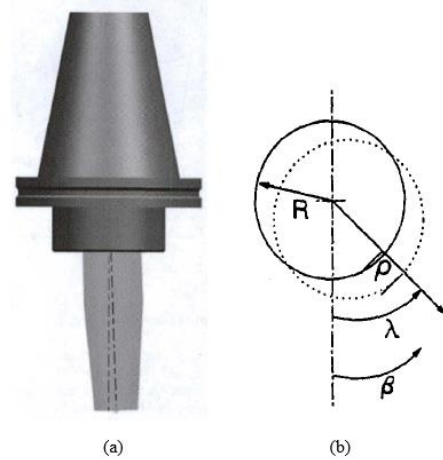


Figure 2. (a) cutting tool with axial run-out [13] (b) cutting tool path with radial run-out [14]

Run-out of the cutting tool has the effect of reducing the precision of defining the cutting forces parameters. Rivière et al. demonstrates the development of a given identification algorithm by modeling the radial run-out effect on the undeformed chip. With the help of simulation, both simple and complex models of the epidemic can predict shear forces [15]. A different approach has been made by Liang et al with a study on real-time chip load compensation to enable more efficient use of machine tools. In this study, the methodology they developed to eliminate cutting force oscillation and machined surface combs due to cutter run-out significantly improved the quality of machined surfaces by reducing their components in the spindle oscillation frequency, as well as the non-asymptotic stable dynamic factors of cutter run-out [16]. In the study using time dependent spectral analysis of shear force in order to estimate the shear run-out properties of force magnitude and angular orientation; The presence of cutter run-out and a cutting force component in the spindle rotation frequency also facilitates run-out monitoring [17]. In addition, mathematical models for cutting geometry, tooth radius, chip thickness, and entry/exit angles were developed by Kline et al. to examine tool run-out. These geometry models are combined with previously developed cutting force models to predict cutter run-out and cutting force characteristics for end milling process. It has been shown that the presence of run-out increases the average chip thickness for the cutting edge actually participating in the cut, it is also increasing the ratio of maximum force to average force [18]. Among the macro-to-micro effects of downscaling in size, tool run-out formation is an important factor that is affecting the cutting force, tool life, and surface integrity of the manufactured part. In conclusion, the precision analysis shows that spindle speeds of less than 5000 rpm in addition to lower run-out lengths guarantee angular errors in tool work [19].

The aim of this study is to create an experimental study on the extent to which the hole drilling operation, which constitutes 40% of the process during machining, affects the production efficiency with the effect of tool run-out and processing in accordance with the desired value after production.

2. Material and Methods

In the experimental study, SAE 1020 steel, which is widely preferred in construction body manufacturing and mould sets in the sheet metal forming sector, was used. The technical specifications of the steel are given in Table 1. With the experimental study to be made in terms of being suitable for surface hardening in the machining of steel and using it in the construction of apparatus and mould sets, the effect of the CNC spindle tool run-out on the hole during the hole drilling operation was investigated.

Surface roughness of tool run-out was measured with Mahr MarSurf PS1 model surface roughness device in a hole drilling operation with a length of 1, 2 and 3 times the drill diameter used in the hole operation; dimensional accuracy was measured with CMM (Coordinate Measuring Machine-Coordinate Measuring System) and its effects on drill wear were examined. The spindle specifications of the HAAS VM3 CNC vertical machining centre processed are given in Table 2. Coolant was used in the experimental study [20]. During the drilling operation, Oemeta brand coolant suitable for general and heavy machining was used. The properties of the coolant and the water used are given in Table 3. The drill bit, tool holder and boring parameters used at the same time are given in Table 4. Cutting parameters are given based on optimum machining conditions, adhering to the values in the product catalogue.

Table 1. Technical specifications of SEA 1020 steel

C	Si max	Mn
0.18-0.25	0.40	0.30-0.60
P max	S max	Sertlik (HB)
0,045	0.045	45-55

In the drilling operation, the effects on the drilling and chip formation during the process with the steel workpiece to be used in the experimental study, which was prepared to drill holes 1, 2 and 3 times the drill diameter, and the spindle with tool run-out were investigated. After the spindle maintenance, the process was repeated with the same processing parameters and material and compared.

Table 2. Spindle specifications of the HAAS VM3 machine

Spindle	Royal
Maximum Speed	12000 rpm
MaximumTorque	122.0 Nm @ 2000 rpm
Conical Code	CT / BT40

After the hole drilling processes, the dimensions of all the holes were measured in the CMM device. The dimensions of the entry-exit ends and the middle of the holes drilled 3 times the drill diameter and ovalities that may be caused by the run-out in the tool were observed. Then, it was cut from the exact axis of the holes with an electro-erosion device and the surface roughness was investigated. Following the drilling operation, the drill used was examined in terms of wear and tool life. These processes were repeated after the machine maintenance without the tool run-out.

Table 3. Coolant and its properties

Brand	Code	Emulsion Ratio (% Refract.)
OEMETA	Unimet 227	%5
Area of Use	Type	Water
General Machining	Semi-Synthetic	*Hardness = 15 °dH *Chloride = 57 ppm *pH = 7.7 *Conductivity = 665 µs/cm

Table 4. Cutting parameters

	f (mm/min)	S (rpm)
Parameters	50	1000
tool	Tool holder	Brand
HSSDIN 338/R-N Ø9.8 mm	Ball set	Machine Tool

Drilling processes during the experimental study are shown in Figure 3 and Figure 4. Again, the tools and holders used during the work are shown in Figure 5. The wear of the drills used by the runout effect was investigated.

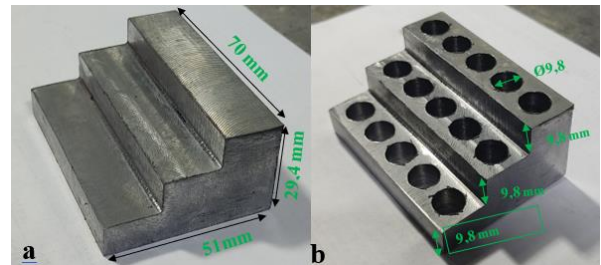


Figure 3. (a) Non-drilled test apparatus (b) Drilled test apparatus (Material SAE 1020)



Figure 4. Drilling operation of the test apparatus



Figure 5. (a) HSS drill Ø 9.8 mm (b) Ball holder and drill

3. Results and discussions

For lengths of 1, 2, and 3 times the drill diameter, pictures of the holes drilled before maintenance and with tool run-out are given in Figure 6. Drilling operations performed by removing tool runouts after maintenance are given in Figure 7. As the hole length increased in the holes drilled while the machine was run-out and not maintained, the burr structures formed in the hole also changed; burr images are given in Figure 7. As the hole length increases, the amount of burrs and burn marks due to overheating are observed in the metal.

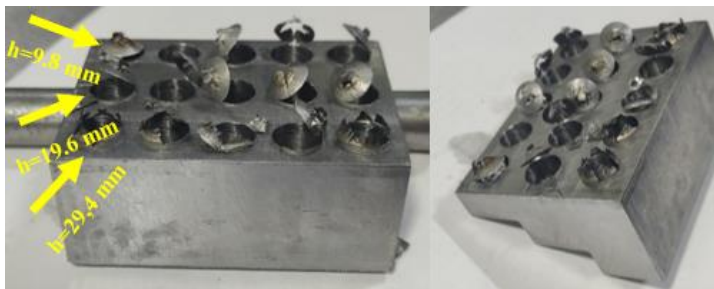


Figure 6. Burr formation that occurs according to the hole length that occurs in the drilled hole operation when there is tool run-out on the machine.

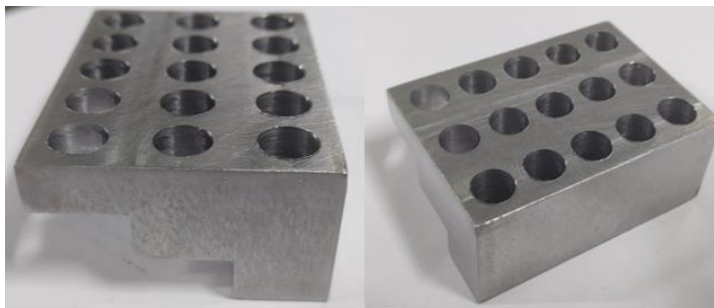


Figure 7. Hole exit images of drilled holes without tool runout after maintenance

After the maintenance, no significant burrs and burn marks were found at the hole exit points. No differences were observed

in the holes according to the hole sizes. The structure of the holes resulted in the desired levels and in accordance with the production after the maintenance.

The hole diameter was measured from the middle of the top hole and the bottom of the hole with a CMM device after the hole operation performed while the bench was run-out before the maintenance. In these measurement results, the dimensions of the hole change in the upper, middle and lower sides. The average of the dimensions of the 5 holes drilled for each length before maintenance is shown in Table 5. The mean of measurements after maintenance work is shown in Table 6. Only the hole length $h=9.8$ mm was not measured from the middle part because the length was short in the middle part of the hole. The diameter larger than the diameter desired to be drilled at the entrance of the hole has approached the desired diameter towards the end of the hole. The large amount of tool run-out at the hole entrance is due to the effect of axial forces that cause run-out, while minimizing axial forces with increasing hole depth causes the amount of run-out to decrease as the hole depth increases. It is gathered from this result that the drill spindle run-out changes the hole diameter. The fact that the holes are not suitable for the Ø 9.8 mm may cause problems that reduce production efficiency such as the loose fitting of the pins that can be used in production, the loss of centering of the moulds over time, the damage of the mould parts, the production of faulty parts due to the failure of their centre fit. After the maintenance, the measurement difference between the dimensions at the bottom of the holes and at the end of holes decreased from an average of 0.3 mm to around 0.01 mm, increasing the linearity of the holes. The degree of rigidity positively affects the life of the pins to be inserted into these holes.

Table 5. According to the hole lengths before maintenance, the average dimensions of the hole diameter at the top, middle and bottom of the hole

Hole diameter Ø	h=29.8mm	h=19.6mm	h=9.8mm
Hole entryAv. Ø	10.118 mm	10.20 mm	10.158 mm
MiddleAv. Ø	10.086 mm	-	-
Hole exitAv. Ø	9.948 mm	9.974 mm	9.994 mm

Table 6. According to the hole lengths after maintenance, the average dimensions of the hole diameter at the top, middle and bottom of the hole

Diameter of Hole	h=29.8mm	h=19.6mm	h=9.8mm
Hole entry Av. Ø	10.366 mm	10.358 mm	10.358 mm
MiddleAv. Ø	10.365 mm	-	-
Hole exitAv. Ø	10.262 mm	10.282 mm	10.204 mm

Before the maintenance, that is, after the drilling operation performed while the machine is running, the diameter of the hole was measured in the middle of the top hole and the roughness Ra was measured with the surface roughness device from the bottom part of the hole. The roughness changes at the top, middle and bottom of the hole. The roughness increased towards the bottom of the hole due to the change in the diameter of the hole above and below the hole and the narrowing of the diameter under the hole. As the drill moves towards the bottom of the hole, it overheats due to the irregular tool friction forces that occur on the tool surface, especially on the cutting edges. With the increasing heat effect of the

material at the bottom of the hole, the plastic behaviour that is facilitated due to the decreasing modulus of elasticity becomes more active, and with the increasing temperature, the cutting process turns into a chip removal mode with more shearing, and this increases the roughness. In addition, the decrease in the cross section of the sub-hole area, especially as drill bit approaches the bottom of the hole, and the increase in temperature make the plastic behaviour an active mechanism and easily deform with the drill advancing forces. Table 7 and Table 8 show the roughness averages of the 5 holes drilled before and after maintenance. Surface roughness measurements made after maintenance produced better results than before the maintenance. The measurement variables in the surface roughness were changed by approximately 30% as shown in the tables. As a result of the comparison of the pre-maintenance values, it is seen that the hole entrance dimensions are higher than the hole exit dimensions.

Table 7. Surface roughness measurements of the top, middle and bottom of the hole (Ra) according to the hole lengths before maintenance

Surface roughness (Ra)	h=29.8mm	h=19.6mm	h=9.8mm
Hole entry Av. Ra	0.8154	1.1454	-
Middle Av. Ra	1.0146	-	1.3634
Hole exit Av. Ra	2.1544	1.5868	-

Table 8. Surface roughness measurements of the top, middle and bottom of the hole (Ra) according to the hole lengths after maintenance

Surface roughness (Ra)	h=29.8mm	h=19.6mm	h=9.8mm
Hole entry Av. Ra	0.7136	1.0476	-
Middle Av. Ra	0.9324	-	0.981
Hole exit Av. Ra	2.0718	1.1045	-

Due to the length of the hole, two measurements were taken from the hole with a length of $h = 19.6$ mm and a single measurement was taken from the hole with a length of $h = 9.8$ mm so that the surface roughness device could make a valid measurement. The surface roughness of the holes and the narrowing of the diameter from the top of the hole to the bottom can be seen in Figure 8.

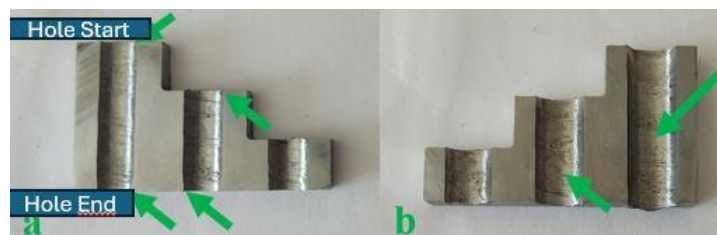


Figure 8. Drilling operation before maintenance; (a) Diameter changes at the top and bottom of the hole (b) Rough surfaces on the hole surface

The formation of the burr height that occurs during drilling when the tool is run-out due to the increase in the hole length can be seen in Figure 9. It was observed that the amount of burr at the bottom of the hole increased as the hole length increased. It is compared with the amount of burr formed after maintenance. Burr formation creates the need for more hand levelling and deburring operations. After the maintenance, no shrinkage or burr formation was observed in the hole.



Figure 9. Hole burr formation due to hole length when tool run-out is present before maintenance

4. Conclusions

In this experimental study, in which the effects of tool run-out on the drilling operation were investigated, tool run-out was measured before maintenance and maintenance was performed afterwards. In maintenance, after the maintenance of the bearings and the tension springs, the tool run-out was reduced from $45\mu\text{m}$ to $8\mu\text{m}$, as measured by the test apparatus, the spindle cone and the test apparatus, together with the conical grinding processes. As a result of the removal of tool run-out, machine efficiency has increased.

After the tool run-out has been removed:

- Surface roughness has improved %30 for hole entry, middle and exit compared to Tables 7 and 8.
- The hole size is produced with %35 less error when compared to the values in Tables 5 and 6.
- At the end of the hole, the burr formation seen in the pre-maintenance hole operation was improved by 20%.
- At the end of the hole, 40% of the surface color change due to heat generated during chip removal, which was observed during the hole operation before the maintenance, disappeared after the maintenance.

Acknowledgment

This study was supported by Bursa Şahinkul Makina R&D Center with the project number ARGE-2022-28 2201100000.

Conflict of Interest Statement

The authors must declare that there is no conflict of interest in the study.

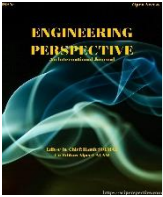
Author Statement

M. Kubilay Askerden: Conceptualization, Supervision, **Mustafa Yazar:** Conceptualization, Writing-original draft, **Şükri Talaş:** Data curation, Validation





References

1. Subramanian, K., & Cook, N. H. (1977). Sensing of drill wear and prediction of drill life. *ASME J. Eng. Ind.*, 99 (2): 295-301
2. Matsumura, T. (2016). Cutting simulation of drilling with cutter runout. In 2016 International Symposium on Flexible Automation (ISFA) (pp.

- 251-254). IEEE.
3. Mary, J. S., Balaji, M. S., Krishnakumari, A., Nakandhrakumar, R. S., & Dinakaran, D. (2019). Monitoring of drill runout using least square support vector machine classifier. *Measurement*, 146, 24-34.
 4. Schmitz, T. L., Ziegert, J. C., Canning, J. S., & Zapata, R. (2008). Case study: A comparison of error sources in high-speed milling. *Precision Engineering*, 32(2), 126-133.
 5. Caixu, Y. U. E., Haining, G. A. O., Xianli, L. I. U., Liang, S. Y., & Lihui, W. A. N. G. (2019). A review of chatter vibration research in milling. *Chinese Journal of Aeronautics*, 32(2), 215-242.
 6. Sakuma, K., Kiyota, H., & Morita, H. (1983). Positional Accuracy of Hole in Drilling: Effect of Rigidity and Point Geometry of Drill. *Bulletin of JSME*, 26 (214), 659-666.
 7. Morales Méndez, J. D., & Rodriguez, R. S. (2017). Total productive maintenance (TPM) as a tool for improving productivity: a case study of application in the bottleneck of an auto-parts machining line. *The International Journal of Advanced Manufacturing Technology*, 92, 1013-1026.
 8. Abele, E., Altintas, Y., & Brecher, C. (2010). Machine tool spindle units. *CIRP annals*, 59 (2), 781-802.
 9. Usop, Z., Sarhan, A. A., Mardi, N. A., & Abd Wahab, M. N. (2015). Measuring of positioning, circularity and static errors of a CNC Vertical Machining Centre for validating the machining accuracy. *Measurement*, 61, 39-50.
 10. Zhang, X., Zhang, J., Zhang, W., Li, J., & Zhao, W. (2018). A non-contact calibration method for cutter runout with spindle speed dependent effect and analysis of its influence on milling process. *Precision Engineering*, 51, 280-290.
 11. Li, H. Z., & Li, X. P. (2005). A numerical study of the effects of cutter runout on milling process geometry based on true tooth trajectory. *The International Journal of Advanced Manufacturing Technology*, 25, 435-443.
 12. Matsumura, T., & Tamura, S. (2017). Cutting force model in milling with cutter runout. *Procedia CIRP*, 58, 566-571.
 13. Li, Z. L., & Zhu, L. M. (2014). Envelope surface modeling and tool path optimization for five-axis flank milling considering cutter runout. *Journal of Manufacturing Science and Engineering*, 136(4), 041021.
 14. Wang, J. J. J., & Liang, S. Y. (1996). Chip load kinematics in milling with radial cutter runout. *ASME. J. Eng. Ind.*, 118(1): 111-116.
 15. Rivière-Lorphèvre, E., & Filippi, E. (2009). Mechanistic cutting force model parameters evaluation in milling taking cutter radial runout into account. *The International Journal of Advanced Manufacturing Technology*, 45, 8-15.
 16. Liang, S. Y., & Perry, S. A. (1994). In-process compensation for milling cutter runout via chip load manipulation. *ASME. J. Eng. Ind.* 116 (2): 153-160.
 17. Hekman, K. A., & Liang, S. Y. (1997). In-process monitoring of end milling cutter runout. *Mechatronics*, 7(1), 1-10.
 18. Kline, W. A., & DeVor, R. E. (1983). The effect of runout on cutting geometry and forces in end milling. *International Journal of Machine Tool Design and Research*, 23(2-3), 123-140.
 19. Attanasio, A. (2017). Tool run-out measurement in micro milling. *Micromachines*, 8(7), 221.
 20. Isik, Y. (2010). An experimental investigation on effect of cutting fluids in turning with coated carbides tool. *J. Mech. Eng.*, 56(3), 195-201.



A Study of Modified Nanofluid Flow Over an Exponentially Stretching Surface With Inclined Magnetic Field and Porous Media

Nikita Jain¹ , Manish Gaur² , Priyanka Agrawal³ , Praveen Kumar Dadheech^{4*} 

¹ Govt. Engineering College Jhalawar, India

² Department of Mathematics, Government PG College, Kota, India

³ Department of Mathematics, University of Rajasthan, Jaipur, India

⁴ Indian Institute of Information Technology Kota, India

ABSTRACT

A numerical study of $Fe_3O_4 - TiO_2 - Ni/C_2H_6O_2$ modified nanofluid's flow through a stretched surface is presented in the current work with an applied angled magnetic field. In the subsequent form of hybrid nanofluid, known as modified nanofluid, three distinct suspended nanoparticles in a base fluid are taken into consideration. Iron Oxide, Nical, and Titanium Dioxide nanoparticles are suspended in ethanol glycol, which is used as a base liquid. One way to improve heat transfer rates in MHD flow over a stretched surface with variable viscosity is to utilize modified nanofluids. This is useful in a number of sectors, including energy systems, thermal management in aircraft, and cooling electronic systems. By applying the proper similarity transformations, the Runga-Kutta fourth order technique encounters the mathematical framework of the flow. One important finding is that, in contrast to nanofluids and hybrid nanofluids, the modified nanofluid has a larger capacity for heat transmission. The modified nanofluid's heat transfer capabilities exhibit intriguing behavior that calls for more research on it. There are numerical solutions that are displayed graphically. Increases in the volume fraction parameter and the inclination angle parameter of the magnetic field have been found to cause a drop in the velocity field of the modified nanofluid.

Keywords: Heat Transfer; MHD; Modified Nanofluid; Porous Media; Stretching Sheet

History

Received: 18.05.2024

Accepted: 27.08.2024

Author Contacts

*Corresponding Author

e-mail addresses : nikitajmaths@gmail.com, manishbhartigaur@gmail.com, prmyfr@gmail.com, dadheechpraveen07@gmail.com*

How to cite this paper:

Jain, N., Gaur, M., Agrawal, P., Dadheech, P.K., (2024). A study of modified nanofluid flow over an exponentially stretching surface with inclined magnetic field and porous media. Engineering Perspective, 4 (3), 125-129. <http://dx.doi.org/10.29228/eng.pers.76434>

1. Introduction

Non-Newtonian fluids have been applied in several industrial processes in recent years. Numerous sectors, including the pharmaceutical, chemical, biological, and petroleum industries, are benefiting from the unique qualities of non-Newtonian fluids. Non-Newtonian fluids have a wide range of uses, which has led to a fast growth in their study. In many industrial applications, regular fluids like water, ethylene-glycol, propylene-glycol, and engine-oil are used for heat transmission. Enhancing these liquids' ability to transport heat can lower the cost of goods, power, processing time, and size, and increase device operating time. The fact that traditional heat exchangers require low temperatures to operate is one issue with heat exchange systems. The thermal conductivity of this liquid may be optimized with the distribution of solid particles. Thermal conductivity of heterogeneous two-components system was investigated by R.

Hamilton [1]. The thermal conductivities of a variety of heterogeneous two-component systems were studied by researchers in 1962. The empirical shape factor, which is dependent on the thermal conductivities of the phases and the included particle's shape, can be determined with accuracy using an equation. A review on nanofluid was written by W. Yu and H. Xie [2]. Preparations and stability factors were discussed by the authors in their review. They also discuss the opportunity for future of nanofluid. Nanofluids square measure dispersion of nano-materials (such as nano-fibers, nano-tubes, nanoparticles nano-rods, nano-wires, nano-sheets, or droplets) in fundamental fluids. Due in large part to the early observations of aberrant thermal physical phenomena (k) advancement of nanofluids with any low fraction of nanoparticles, nanofluids have garnered considerable interest over the past ten years. With numerous reports of unusual improvements in thermal physical phenomena and numerous

Table 1. Thermo-physical characteristics of modified nanofluid: [8,10]

$\mu_{mnf} = \frac{\mu_f}{(1 - \phi_1)^{2.5}(1 - \phi_2)^{2.5}(1 - \phi_3)^{2.5}}$	Effective dynamic viscosity
$\rho_{mnf} = (1 - \phi_3) \left\{ [(1 - \phi_1)\rho_f + \phi_1\rho_{s1}](1 - \phi_2) \right\} + \phi_2\rho_{s2} + \phi_3\rho_{s3}$	Effective density
$\sigma_{mnf} = \frac{2\sigma_{hnf} + \sigma_{s3} - 2(\sigma_{hnf} - \sigma_{s3})\phi_3}{2\sigma_{hnf} + \sigma_{s3} + (\sigma_{hnf} - \sigma_{s3})\phi_3} \sigma_{hnf}$ where $\sigma_{hnf} = \frac{2\sigma_{nf} + \sigma_{s2} - 2(\sigma_{nf} - \sigma_{s2})\phi_2}{2\sigma_{nf} + \sigma_{s2} + (\sigma_{nf} - \sigma_{s2})\phi_2} \sigma_{nf}$ and $\sigma_{nf} = \frac{\sigma_{s1} + 2\sigma_f - 2\phi_1(\sigma_f - \sigma_{s1})}{\sigma_{s1} + 2\sigma_f + \phi_1(\sigma_f - \sigma_{s1})} \sigma_f$	Electrical conductivity
$\kappa_{mnf} = \frac{\left\{ \frac{\kappa_{s3} + (n-1)\kappa_{hnf} - (n-1)(\kappa_{hnf} - \kappa_{s3})\phi_3}{\kappa_{s3} + (n-1)\kappa_{hnf} + (\kappa_{hnf} - \kappa_{s3})\phi_3} \right\} \kappa_{hnf}}{\left\{ \frac{\kappa_{s2} + (n-1)\kappa_{nf} - (n-1)(\kappa_{nf} - \kappa_{s2})\phi_2}{\kappa_{s2} + (n-1)\kappa_{nf} + (\kappa_{nf} - \kappa_{s2})\phi_2} \right\} \kappa_{nf}}$ $\kappa_{nf} = \frac{\left\{ \kappa_{s1} + (n-1)\kappa_f - (n-1)(\kappa_f - \kappa_{s1})\phi_1 \right\} \kappa_f}{\left\{ \kappa_{s1} + (n-1)\kappa_f + (\kappa_f - \kappa_{s1})\phi_1 \right\}}$	Thermal conductivity
$(\rho C_p)_{mnf} = (1 - \phi_3) \left\{ (1 - \phi_2) \left[(1 - \phi_1)(\rho C_p)_f + (\rho C_p)_{s1} \phi_1 \right] + (\rho C_p)_{s2} \phi_2 \right\} + \phi_3(\rho C_p)_{s3}$	Heat capacitance

Table 2 Thermo-physical values: [2, 6, 7, 11]

	ρ (kg /m ³)	C_p (J /kg K)	k (W /m K)	σ (S/m)
$C_2H_6O_2$	1116.6	2382	0.249	0.01485
Fe_3O_4	5200	670	9.8	0.74×10^6
Ni	8900	444	90.7	1.7×10^7
TiO_2	4175	692	8.4	6.27×10^{-5}

2.1. Similarity transformation

To solve our model, we apply the similarity transformation below[11]:

$$u = U_0 e^{\frac{x}{l}} f'(\eta), v = -\sqrt{\frac{\nu_f U_0}{2l}} e^{x/2l} [f(\eta) + \eta f'(\eta)]$$

$$\text{and } (\eta) = \frac{T - T_\infty}{T_w - T_\infty} \tag{5}$$

Where $\eta = y \sqrt{\frac{U_0}{2lv_f}} e^{x/2l}$ and using the aforementioned transformations, the nonlinear equations of the flow have been incorporated into the subsequent ordinary differential equations.

$$A f''' + B(f f'' - 2f'^2) - \frac{\sigma_{mnf}}{\sigma_f} M \sin^2 \alpha f' = 0. \tag{6}$$

$$\frac{1}{Pr} \frac{\kappa_{mnf}}{\kappa_f} C \theta'' + f \theta' - f' \theta = 0. \tag{7}$$

Here

$$A = \frac{1}{(1 - \phi_1)^{2.5}(1 - \phi_2)^{2.5}(1 - \phi_3)^{2.5}},$$

$$B = (1 - \phi_3) \left\{ (1 - \phi_2) \left[(1 - \phi_1) + \phi_1 \frac{\rho_{s1}}{\rho_f} \right] \right\} + \phi_2 \frac{\rho_{s2}}{\rho_f} + \phi_3$$

and

$$C = \left[(1 - \phi_3) \left\{ (1 - \phi_2) \left[(1 - \phi_1) + \phi_1 \frac{(\rho C_p)_{s1}}{(\rho C_p)_f} \right] \right\} + \phi_2 \frac{(\rho C_p)_{s2}}{(\rho C_p)_f} + \phi_3 \frac{(\rho C_p)_{s3}}{(\rho C_p)_f} \right]^{-1}$$

Boundary condition (5) is also modified using the aforementioned transformations as:

$$\theta(0) = 1, f(0) = 0, f'(0) = 1, \theta(\infty) = 0, f'(\infty) = 0. \tag{8}$$

Where $M = \frac{2l B_0^2 \sigma_f}{U_0 \rho_f e^{x/l}}$ is Magnetic parameter, $Pr = \frac{(\rho C_p)_f \nu_f}{\kappa_f}$ is

Prandtl number. An additional physical measure is the local Nusselt number, which is provided by

$$Nu_x = -\left(\frac{\kappa_{hnf}}{\kappa_f} + \frac{4R}{3} \right) \psi_1 x \theta'(0). \tag{9}$$

3. Numerical Solution

Moreover, Eq. (6) and Eq. (7) and boundary conditions Eq. (8) have been recast as first-order initial value problems, using the following definitions:

$$f' = h_2, f'' = h_3, \theta = h_4, \theta' = h_5, h'_3 = \frac{B}{A} (2h_2^2 - h_1 h_3) +$$

$$\frac{M \sigma_{mnf}}{A \sigma_f} h_2 \sin^2 \alpha \text{ and } h'_5 = \frac{Pr \cdot \kappa_f}{C \kappa_{mnf}} (h_2 h_4 - h_1 h_5).$$

With boundary condition, $h_1(0) = 0, h_2(0) = 1, h_3(0) = 1, h_4(0) = 1.$

For numerical solutions these ODE's are converted into first ordered IVP. In this IVP only three initial conditions are present, but five are required for the solution as $h_3(0)$ and $h_5(0)$. Assuming the initial guess values for $h_3(0)$ and $h_5(0)$ and suitable finite value of $\eta(\rightarrow \infty)$, say η_∞ numerical solutions by Runge-Kutta method are obtained. Then computations for $f'(\eta)$ and $\theta(\eta)$ at $\eta_\infty (\cong 10)$ along with conditions of boundary $f'(\eta_\infty) = 0$ and $\theta(\eta_\infty) = 0$ are performed. Approximated (degree of accuracy is 10^{-6}) solutions have obtained by adjusting the values of $f''(0)$ and $\theta'(0)$ by considering step size $\Delta \eta = 0.01$. This technique uses an iterated strategy to provide accurate findings up to 10^{-7} accuracy.

4. Result and Discussions

The flow characterization through an exponentially stretched sheet of modified nanofluids is investigated. Various inclination angles are used while applying a magnetic field. Further, the variation of several contributing parameters on the fluid velocity and temperature profiles are presented via graphs.

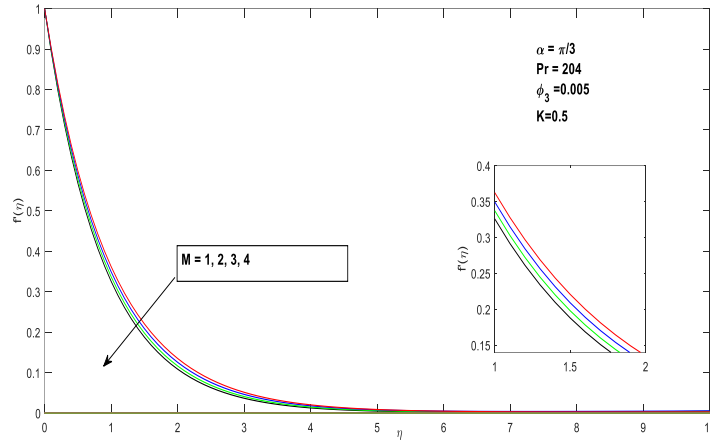


Figure 2. Velocity profile for the magnetic field parameter M.

The consequence of M on $f'(\eta)$ for the modified nanofluid $Fe_3O_4 - Ni - TiO_2/C_2H_6O_2$ is shown in Figure 2. The velocity profile decreases as M increases, according to the findings. The magnetic field produced by the movement of an electrically conducting fluid creates a Lorentz force, which has the retardation feature. This is the reason for the diminishing appearance of the velocity profile. As M rises, the retardation strength of all the three nanofluids grows. As a result, velocity decreases as well.

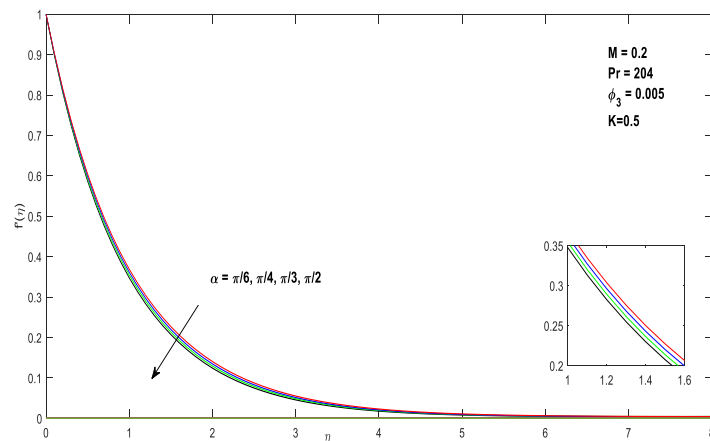


Figure 3. Velocity profile for the inclination angle parameter α .

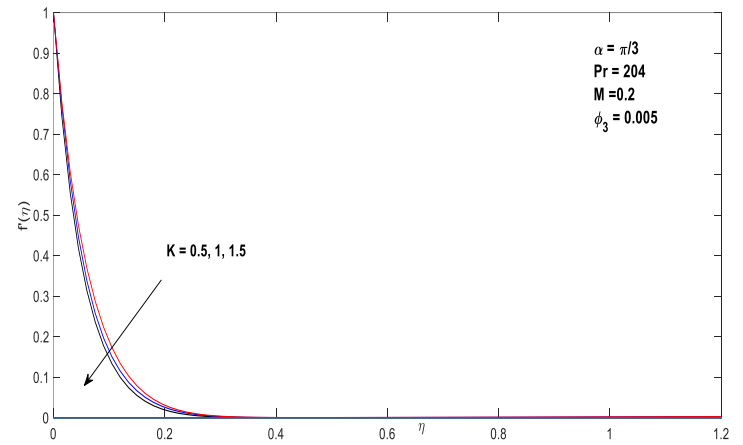


Figure 4. Velocity profile for the permeability parameter K.

Figure 3 shows the impact of the α on $f'(\eta)$. When the parameter is increased, the $f'(\eta)$ profile falls. This is due to the fact that as the angle of inclination increases, the magnetic field becomes stronger and the Lorentz force reduces the velocity field. The influence of the permeability parameter K on the velocity profile is illustrated in Figure 4. A distinct decline in velocity within the flow pattern is noticed. The impact of volume friction ϕ_3 on $f'(\eta)$ is shown in Figure 5.

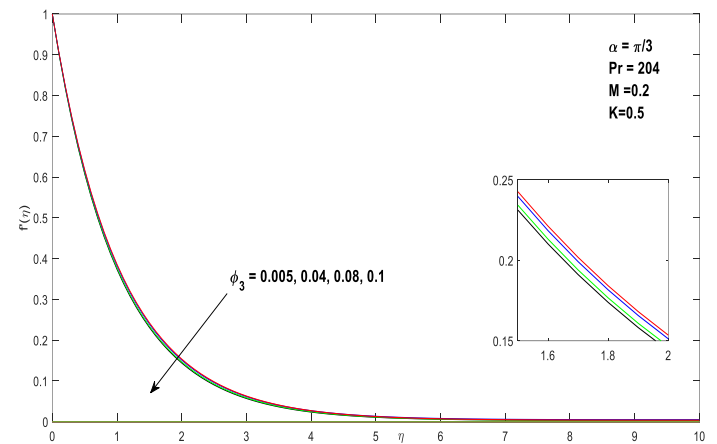


Figure 5. Velocity profile for the parameter ϕ_3 .

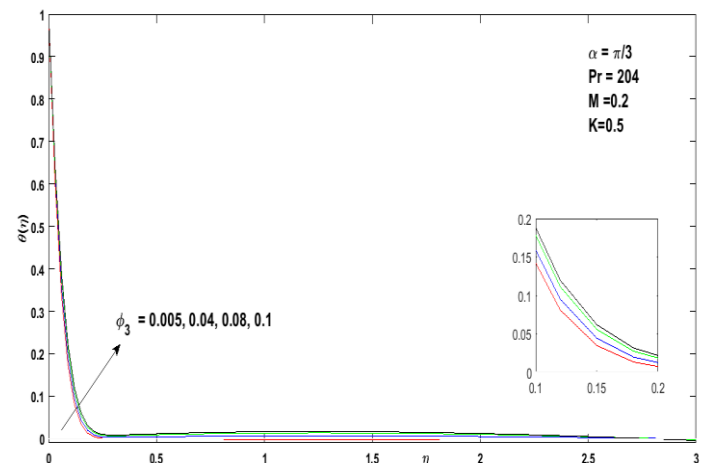


Figure 6. Temperature profile for the parameter ϕ_3 .

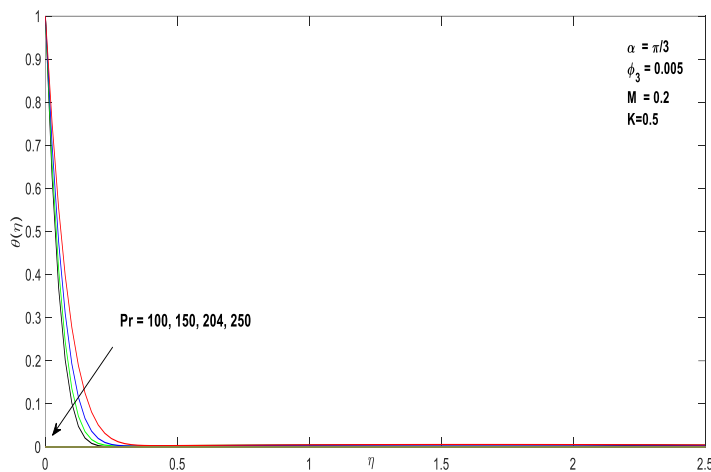


Figure 7. Temperature profile for the parameter ϕ_3 .

It is seen that a drop in the velocity profile occurs with an increase in ϕ_3 . Additionally, it is noted for ϕ_3 that the fluid's speed increases with increasing ϕ_3 away from the sheet and decreases in its immediate vicinity. Figure 6 illustrates how ϕ_3 affects $\theta(\eta)$.

It has been shown that for changed nanofluids, an enhanced temperature profile results from increased ϕ_3 . A higher temperature field may arise from the extraction of more energy from a greater number of nanoparticles. The influence of Pr on $\theta(\eta)$ is shown in Figure 7. The figures indicate that a reduction in the temperature profile $\theta(\eta)$ is noticed with an increase in Pr.

5. Conclusions

The impact of heat transfer of modified nanofluids flowing past an exponentially extending surface under the influence of an applied angled magnetic field has been studied. A modified nanofluid composed of ethylene glycol that contains a suspension of $Fe_3O_4 - TiO_2 - Ni$ nanoparticles have been visually displayed. By applying the proper similarity transformations, the Runge-Kutta fourth order technique solves the flow's governing models.

The key results that follow are achieved.

- A decrease in the velocity field has been observed for the modified nanofluid with an increase in the inclination angle and magnetic field parameter.
- The velocity curve for ϕ_3 shows that the fluid velocity increases away from the sheet and reduces toward the wall.
- A decrease is observed with an increase in the velocity field's ϕ_3 , but a reversal of this impact is shown in the temperature profile.

Acknowledgment

The authors would like to thank anonymous referees and editor for their useful critical comments and suggestions for improving the research paper.

Conflict of Interest Statement

The authors declare that there is no conflict of interest in the study.

CRediT Author Statement

N. Jain: Conceptualization, Mathematical modeling, Writing-original draft **M. Gaur:** Conceptualization, Supervision **Priyanka Agrawal:** Validation, Software, result analysis **P.K. Dadheech:** Data curation, Formal analysis, revisions.

References

1. Hamilton, R. L., & Crosser, O. K. (1962). Thermal conductivity of heterogeneous two-component systems. *Industrial & Engineering chemistry fundamentals*, 1(3), 187-191.
2. Yu, W., & Xie, H. (2012). A review on nanofluids: preparation, stability mechanisms, and applications. *Journal of nanomaterials*, 2012(1), 435873.
3. Hemmat Esfe, M., Saedodin, S., Wongwises, S., & Toghraie, D. (2015). An experimental study on the effect of diameter on thermal conductivity and dynamic viscosity of Fe/water nanofluids. *Journal of Thermal Analysis and Calorimetry*, 119, 1817-1824.
4. Imtiaz, M., Hayat, T., Alsaedi, A., & Ahmad, B. (2016). Convective flow of carbon nanotubes between rotating stretchable disks with thermal radiation effects. *International journal of heat and mass transfer*, 101, 948-957.
5. Chamkha, A. J., Dogonchi, A. S., & Ganji, D. D. (2019). Magneto-hydrodynamic flow and heat transfer of a hybrid nanofluid in a rotating system among two surfaces in the presence of thermal radiation and Joule heating. *Aip Advances*, 9(2).
6. Acharya, N., Maity, S., & Kundu, P. K. (2020). Influence of inclined magnetic field on the flow of condensed nanomaterial over a slippery surface: the hybrid visualization. *Applied Nanoscience*, 10(2), 633-647.
7. Waini, I., Ishak, A., & Pop, I. (2019). Flow and heat transfer along a permeable stretching/shrinking curved surface in a hybrid nanofluid. *Physica Scripta*, 94(10), 105219.
8. Dadheech, P. K., Agrawal, P., Mebarek-Oudina, F., Abu-Hamdeh, N. H., & Sharma, A. (2020). Comparative heat transfer analysis of MoS₂/C₂H₆O₂ and SiO₂-MoS₂/C₂H₆O₂ nanofluids with natural convection and inclined magnetic field. *Journal of Nanofluids*, 9(3), 161-167.
9. Nadeem, S., & Abbas, N. (2019). Effects of MHD on modified nanofluid model with variable viscosity in a porous medium. *Nanofluid Flow in Porous Media*, 7.
10. Abbas, N., Nadeem, S., & Issakhov, A. (2021). Transportation of modified nanofluid flow with time dependent viscosity over a Riga plate: exponentially stretching. *Ain Shams Engineering Journal*, 12(4), 3967-3973.
11. Dadheech, P. K., Agrawal, P., Sharma, A., Nisar, K. S., & Purohit, S. D. (2021). Transportation of Al₂O₃-SiO₂-TiO₂ modified nanofluid over an exponentially stretching surface with inclined magnetohydrodynamic. *Thermal Science*, 25(Spec. issue 2), 279-285.